UCRL-52142

DESIGN STUDY OF ELECTROSTATICALLY PLUGGED CUSP FUSION REACTOR

Thomas J. Dolan

November 1, 1976

Prepared for U.S. Energy Research & Development Administration under contract No. W-7405-Eng-48

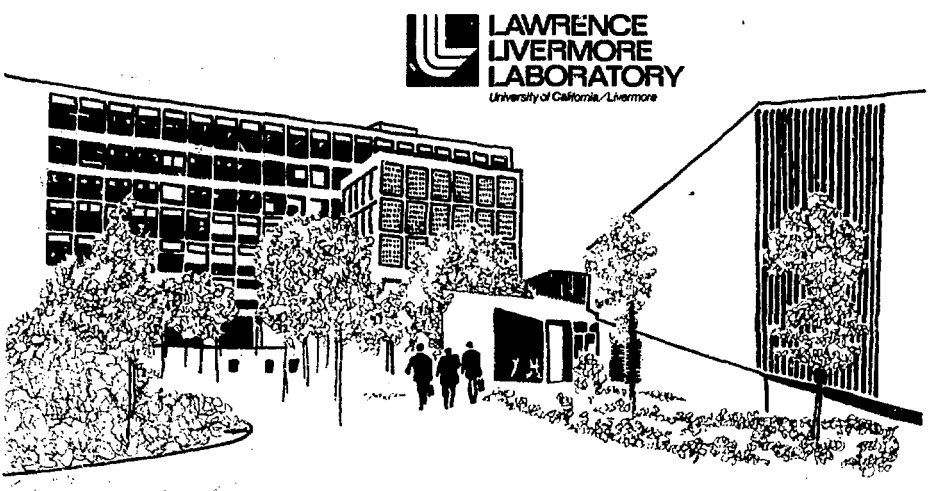

Printed in the United States of America
Available from
National Technical Information Service
U.S. Department of Commerce
5285 Port Royal Road
Springfield, VA 22161
Price: Printed Copy $; Microfiche $2.25

Page Range	Domestic Price	Page Range	Domestic Price
001–025	$ 3.50	326–350	10.00
026–050	4.00	351–375	10.50
051–075	4.50	376–400	10.75
076–100	5.00	401–425	11.00
101–125	5.50	426–450	11.75
126–150	6.00	451–475	12.00
151–175	6.75	476–500	12.50
176–200	7.50	501–525	12.75
201–225	7.75	526–550	13.00
226–250	8.00	551–575	13.50
251–275	9.00	576–600	13.75
276–300	9.25	601–up	*
301–325	9.75		

*Add $2.50 for each additional 100 page increment from 601 to 1,000 pages: add $4.50 for each additional 100 page increment over 1,000 pages.

Distribution Category
UC-20

LAWRENCE LIVERMORE LABORATORY
University of California Livermore, California 94550

UCRL-52142

DESIGN STUDY OF ELECTROSTATICALLY PLUGGED CUSP FUSION REACTOR

Thomas J. Dolan

MS. date: August 18, 1976

MASTER

Contents

DESIGN STUDY OF ELECTROSTATICALLY PLUGGED CUSP FUSION REACTOR

Abstract

This study concentrates on the following aspects of an electrostatically plugged cusp reactor that will be different from other fusion reactor designs: the coil geometry and structural supports, high voltage electrodes, plasma parameters, power balance, and operating cycle. Assuming the electron density distribution in the anodes to have a characteristic width of two electron Larmor radii, which is consistent with present experimental results, the theory predicts that a device with a magnetic field strength, B = 8 T sustained solely by electron beam injection at 300 kV will have a power gain ratio, Q, of about 5. A toroidal multipole cusp configuration with six cusps was selected for the present design, based on a study of the ratio of plasma volume to coil volume. Coil forces are sustained by cryogenic trusses between like coils, fiberglass compression columns, and room temperature hoops. Radiation collimators in front of the high voltage electrodes greatly reduce the radiation impinging on the cathodes, helping to avoid breakdown and to prolong insulator life. The operating cycle consists of a startup period of about 20 s, followed by a fusion burn period lasting about 200 s (limited by impurity buildup) and a 20-s flushing period.

Introduction

Plugging Electrodes and Electrostatic Potential Variation

Charged particles in a high-beta cusp plasma will travel in straight lines until they come to the plasma boundary, where they are reflected off the magnetic wall, as illustrated in Fig. 1. Only those particles travelling in the right direction will pass out through the cusp. This particle reflection, called "geometric mirroring," permits the particles to make hundreds of transits through the central region before going out one of the cusps. Nevertheless, because even thousands of transit times constitute too short a time for adequate plasma confinement, some additional confinement technique is needed to reflect those particles that pass out through the cusps.

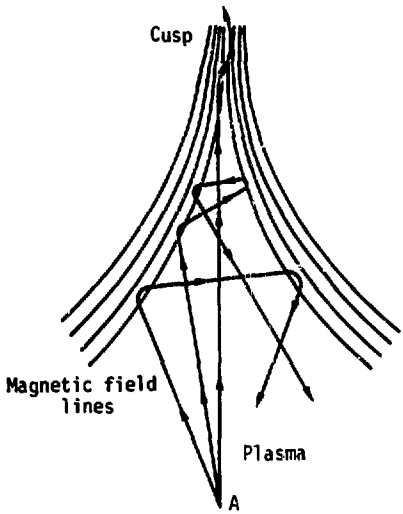

Fig. 1. Charged particle trajectories in a high-beta plasma confined by cusped magnetic field (many of the particles starting out at point A will be reflected by converging magnetic walls).

One technique for reducing particle losses is to apply an electrostatic field parallel to the magnetic field lines in the cusp regions.[1,2] The electrodes used with a spindle cusp are illustrated in Fig. 2. Two circular coils with opposite currents produce the magnetic field illustrated by the dotted lines. A high negative voltage is applied to the cathodes to repel escaping electrons, and the anodes are usually grounded. Plasma may be produced by electron beam injection or any other means. At first some ions are easily lost along the magnetic field lines, but the electrons will be confined by the magnetic field and the negative plugs. After a few ions are lost, the plasma develops a negative potential relative to the grounded anodes, due to the deficit of ions and excess of electron space charge. The axial variation of potential then looks like the smooth curve of Fig. 3. Ions are confined in a negative electrostatic potential well, and they must have energies greater than the ion potential barrier, ϕ_i, in order to escape along magnetic field lines. The potential inside the anodes is depressed an amount $\Delta\phi$ by the electron space charge, which limits the allowable electron density there. In order to keep $\Delta\phi$ small at high electron density, the width of the anode gaps must be kept small ($\sim$3 mm or less). The potential $\phi(r,z)$ inside the anodes is saddle-shaped, as illustrated in Fig. 4, and $\Delta\phi$ represents the difference in potential between the saddle point and the anode. The magnitude

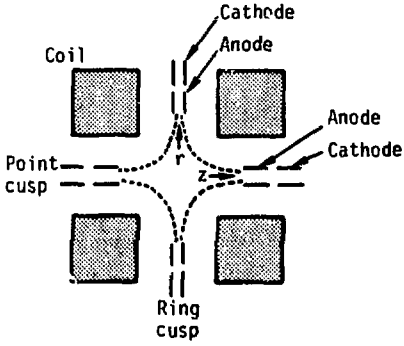

Fig. 2. Circular spindle cusp coils (shaded areas) and associated plugging electrodes (dotted lines represent magnetic field lines).

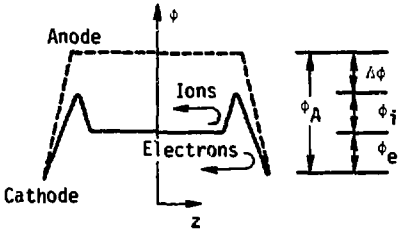

Fig. 3. Axial variation of electrostatic potential for spindle cusp of Fig. 2 (dashed line is for case without plasma, and smooth curve is with plasma; curved arrows indicate charged particle reflection by electrostatic barriers ϕ_i and ϕ_e).

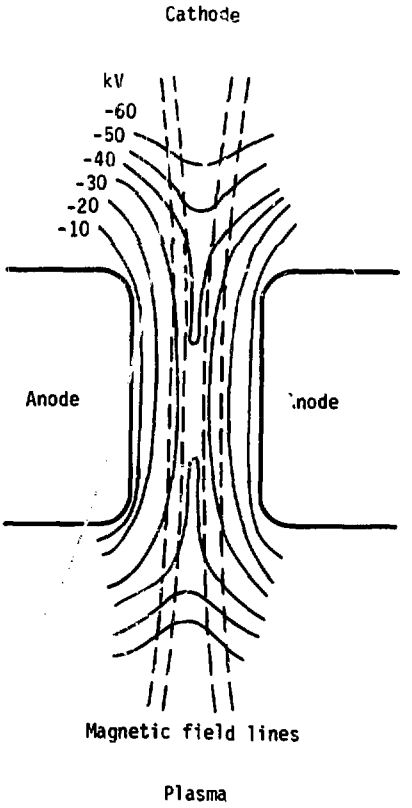

Fig. 4. Equipotential surfaces in anode region, showing saddle shape of electrostatic potential (width of anode gap is exaggerated for clarity, and voltages are hypothetical, for case in which $\Delta\phi$ = 35 kV).

of $\Delta\phi$ is found in the Theory section under Anode Potential Drop for an assumed electron density profile.

Electrons are repelled by a potential barrier, ϕ_e. The applied voltage, ϕ_A, is equal to $\phi_e + \phi_i + \Delta\phi$. The magnitu[illegible] of the potentials automatically

adjust themselves so that the electron and ion densities are nearly equal. For example, if the potential well for ions, ϕ_i, becomes too large, ion losses will be greatly reduced, and the ion density will increase. This increase in n_i will drive the plasma potential more positive, reducing ϕ_i. Thus, the magnitudes of the potentials can be predicted analytically, given equations for the loss rates as functions of the potential barriers.[3]

Particle Loss Processes

Primary electrons are injected into the confinement region from electron guns at the cathodes, and secondary electrons are produced by ionization of residual gas. Ions are produced by ionization.

Ions cannot be lost by diffusion across the magnetic field: they would have to overcome an electrostatic potential barrier of $(\phi_i + \Delta\phi)$ in order to reach the walls. However, they can be lost along magnetic field lines when they acquire energies greater than ϕ_i. Ions with energies greater than ϕ_i are lost out of the cusps after a few hundred bounce times inside the bottle. This time is far too short for them to acquire enough energy to reach the walls. The dominant ion loss mechanism is by diffusion in velocity space over the ion potential barrier, ϕ_i.

Electrons are lost by classical diffusion across the magnetic field, by diffusion in velocity space over the electron potential barrier, ϕ_e, by trapping in the anode regions with subsequent spatial diffusion, and by recombination. Recombination is probably negligible at high temperatures.

Electron loss to the cathodes is beneficial, because it reduces the current drawn from the cathode power supply. The net cathode current is equal to the primary injection current minus the current of electrons that escape by overcoming the potential barrier, ϕ_e. Only this net current need be considered in computing plasma parameters.

The rate of spatial diffusion of electrons across the magnetic field is calculated in the Theory section under Spatial Diffusion. Since most of the plasma is located in a region of zero magnetic field, this diffusion occurs in a thin boundary around the edges. Although the diffusion rate through this thin layer is fast, the small surface-to-volume ratio permits long characteristic times for loss of electrons by diffusion.

The remaining electron loss mechanism, trapping in the anodes, is the most difficult to calculate. Electron diffusion in velocity space is governed by Coulomb collisions, which can be described by the Fokker-Planck equation.

However, the problem at hand involves (1) at least two velocity components ($v_{\parallel}$ and $v_{\perp}$), (2) an unusual distribution of the magnetic field, which is strong around the edges and zero throughout most of the plasma, producing nonadiabatic orbits in some regions and adiabatic orbits in others, and (3) strong variations of the electrostatic potential, which in turn is governed by the particle distributions. Because of the complexity of the problem, the theoretical descriptions so far are inadequate.

The velocity-diffusion loss rate over the electron potential barrier, τ_e, to the cathodes has been estimated by the Soviet group[4] and by the Canadian group.[5] And the probability of plasma electrons entering the magnetic gaps and reaching the anode regions has been studies by the Soviet group.[6]

The rate of electrostatic trapping and detrapping of electrons in the anode regions is very important for fusion reactor applications; the spatial distribution of these electrons determines the amount of potential "sag," $\Delta\phi$, between the anodes. The loss rate of the injected electrons by electrostatic trapping influences the required input current and power from the cathode power supply. The trapped electron density is estimated in the Theory section under Trapped Electrons.

Heating and Energy Loss Mechanisms

Other heating methods may be applied to electrostatically plugged cusps, but only electron beam injection is studied here. The primary electrons from the cathodes ionize the fuel gas to heat the resulting plasma collisionally. The classical Coulomb collision rates are adequate, because of the long confinement times. In addition to collisional heating by electrons, ions are also heated by acceleration: neutral gas is ionized along the potential slope, and the resulting ions are accelerated as they fall inwards down the potential hill. A slight amount of heating is produced by fusion product alpha particles, but this heating is probably negligible because of the short confinement times of the alpha particles. The alpha particle confinement time can be considerably improved by using a more complex magnetic field geometry (such as by adding a strong toroidal field to the present toroidal multipole cusp), but such improvement is beyond the scope of the present study.

The plasma loses energy by the particle loss mechanisms, by charge exchange, by bremsstrahlung, recombination, and line radiation (from impurities) and by electronic heat conduction (ions cannot reach the walls).

Cyclotron radiation is negligible, because most of the plasma is in a region of low magnetic field.

In order for electrostatic plugging to succeed, the following conditions must exist in the anode regions:

1. The electron density distribution, $n_e(x,y)$, must have a very narrow peak, with a width about two electron Larmor radii. If the peak is much wider than that, the potential sag, $\Delta\phi$, becomes too large, and ion confinement is spoiled. This condition evidently exists in present experiments, which have small $\Delta\phi$ and good hot-ion confinement.[1]

2. The density of anode-trapped electrons must be small. This density is small in present experiments, as indicated by good hot-ion confinement and by measurements of electron energy spectra.[1] The theoretical estimate in the Theory section under Trapped Electrons is consistent with this condition.

3. Electron diffusion in the boundary layer should be at nearly the classical rate, which is consistent with experimental measurements.[7]

In what follows, it is assumed that these conditions exist in the fusion reactor anode regions.

The present theoretical description consists of global particle and energy conservation equations together with an equation for the electrostatic potential. These equations will be discussed in the Theory section under Conservation Equations. The potential sag, $\Delta\phi$, in the anodes, the spatial diffusion time, τ_H, and the electron trapping time, τ_t, will be estimated in the Theory section under Anode Potential Drop, Spatial Diffusion, and Trapped Electrons, respectively, as inputs to these conservation equations. The resulting reactor parameters are summarized in Appendix A.

Theory

Anode Potential Drop

The anodes are illustrated in Fig. 5. The y direction is chosen parallel to the magnetic field lines, which run from the plasma through the anodes to the cathode. The anticipated electron density distribution in the x direction is illustrated at the bottom of the figure. Electrons from the nonadiabatic plasma region streaming into the cusp gaps are constrained by the converging magnetic field to a width of about $2\rho_e$, where ρ_e is the average electron Larmor radius. The electron density distribution, $n_e(x,y)$, varies only

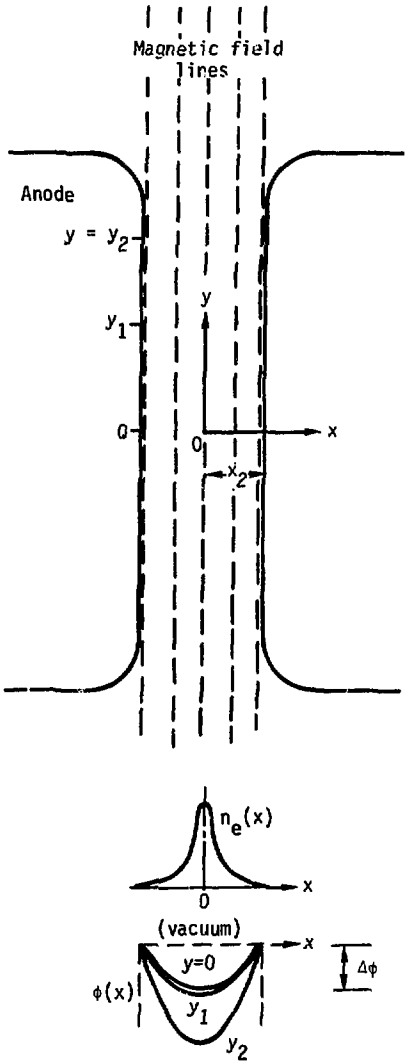

Fig. 5. Anode region in cusp gap, showing magnetic field lines, electron density distribution, and potential distribution as functions of x.

slightly in the y direction inside the anodes. If the length of the anodes in the y direction is much greater than the width of the anode gap $2x_2$, then the potential distribution, $\phi(x,y_1)$, is about the same as $\phi(x,0)$. End effects are observed at y_2, but the potential sag, $\Delta\phi$, which limits ion confinement, can be found from a one-dimensional solution of the Poisson equation for $\phi(x)$ at $y = 0$, as pointed out by Ware and Faulkner, who used a triangular $n_e(x)$.[8]

Here it will be assumed that $n_e(x)$ has a Lorentzian shape given by:

$$n_e(x) = \frac{n_A}{1 + (x/b)^2} , \qquad (1)$$

where b is a variable parameter. The true $n_e(x)$ has neither been computed self-consistently with particle diffusion rates nor measured experimentally. Computation of $n_e(x)$ in the anode regions, taking into account diffusion across the magnetic field with enhancement by diocotron oscillations, diffusion in velocity space with electrostatic trapping of cold electrons, ionization, recombination, distribution of neutral atom density, etc., is the most important remaining theoretical problem.

The solution of the Poisson equation for the distribution of Eq. (1), with the boundary conditions $\phi(\pm x_2) = 0$, is:

$$\Delta\phi \equiv -\phi(0) = (\pi n_A e b x_2/2\varepsilon_0) \left[(2/\pi)\tan^{-1}(x_2/b) - (b/\pi x_2)\ln(1 + x_2^2/b^2)\right] , \qquad (2)$$

where e and ε_0 are the electronic charge and the permittivity of free space, respectively. As discussed in the Introduction under Heating and Energy Loss Mechanisms, we will assume that the width of the electron density distribution in the anode regions is about two electron Larmor radii, so that $b \approx \rho_e$. We choose the anode gap width $2x_2$ to be 3 ± 1 mm. To be conservative, we will use the larger value of 4 mm (x_2 = 2 mm) in calculating $\Delta\phi$, and we will use the minimum gap width of 2 mm in calculating electron diffusion loss rates in the next section. This evaluation takes into account the possibility of anode warpage both increasing $\Delta\phi$ and decreasing diffusion lifetimes.

Because $x_2/b \gg 1$, Eq. (2) simplifies to:

$$\Delta\phi \simeq \frac{\pi n_A e \rho_e x_2}{2\varepsilon_0}\left[1 - \frac{2\rho_e}{\pi x_2}\ln\left(\frac{x_2}{\rho_e}\right)\right] . \qquad (3)$$

The values of $\Delta\phi$ obtained from Eq. (3) are about 1.6 times the values found from the narrow triangular distribution assumed by Ware and Faulkner.[8] If the electron distribution were parabolic, with its zero at the anodes, $\Delta\phi$ would be much larger than the value of Eq. (3), and electrostatic plugging would fail. However, the success of electrostatic plugging experiments thus far indicates that such a distribution does not occur, at least up to plasma densities of a few times 10^{18} m^{-3}.[1]

Spatial Diffusion

The characteristic loss time by diffusion for electrons is the sum of the time for them to be trapped in the magnetic field plus the time to diffuse to the walls after being trapped. According to Lavrent'ev, the magnetic trapping time is on the order of $r_p/\rho'_e\nu_{ei}$, where r_p is the plasma radius, ρ'_e is the electron Larmor radius at the plasma-magnetic field boundary, and ν_{ei} is the electron-ion collision frequency.[9]

Here we will calculate the time it takes electrons to diffuse to the walls after they have been captured by the magnetic field. A toroidal multipole cusp system, which will be described further in the Magnet Coils section, is shown in Fig. 6. In a vacuum, the magnetic field lines fill the chamber, as illustrated in Fig. 7(a), for one segment, and the magnitude of the magnetic field increases almost linearly with radius — Fig. 7(b). In the presence of a high-beta plasma, the magnetic field lines are pushed outwards, as illustrated in Fig. 7(c). Now the magnetic field is zero inside the plasma, and it rises steeply in a boundary layer at the edge of the plasma — Fig. 7(d).

Electrons flying into the cusps from the plasma will have access to a region about $2\rho_e$ wide before they start diffusing. We define the innermost flux surface, ψ_0, as that surface passing a distance ρ_e on either side of the midplane of a cusp, where ρ_e is the average electron Larmor radius in the cusp, as illustrated in the anode region detail of Fig. 8. Electrons will be lost when they reach the outermost flux surface, called ψ_1, which intersects the anodes. The local distance between ψ_0 and ψ_1 is called ξ_1.

The characteristic time for electron loss by spatial diffusion is defined:

$$\tau_d = \frac{\text{(total number of electrons present)}}{\text{(number lost per second by diffusion)}} = \frac{\int dV\, n_e}{\int d\vec{S}\cdot(-D\vec{\nabla}n_e)}, \qquad (4)$$

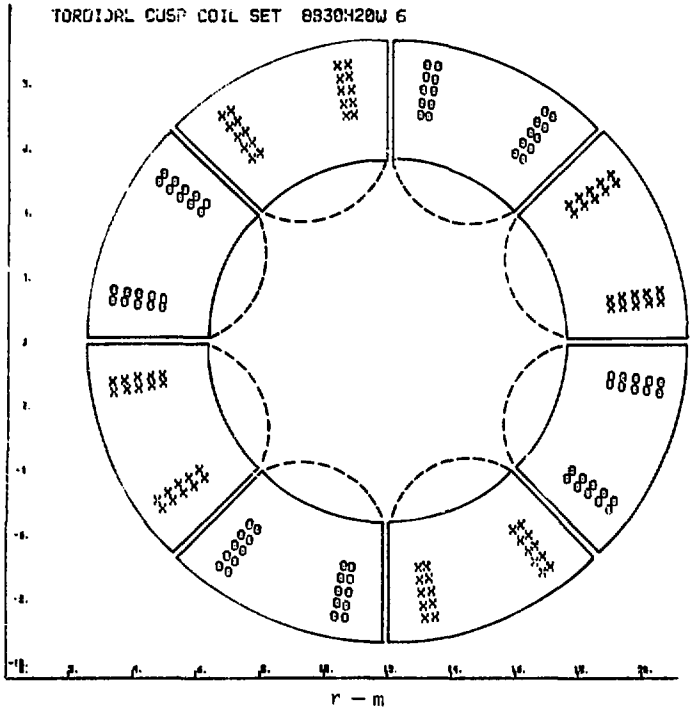

Fig. 6. Cross-sectional view of toroidal multipole coils with N = 8 cusps, B = 3.0 m, h = 2.0 m, and w = 0.6 m; symbols X and O represent coil currents into and out of plane of drawing (dimensions are in metres).

where dV and dS are volume and surface elements. For simplicity, we consider a linear geometry with length L perpendicular to the plane of Fig. 8. Then:

$$dS = Ld\ell, \tag{5}$$

$$\int dV\, n_e = n_0 L\pi r_p^2 , \tag{6}$$

where $d\ell$ is along a magnetic field line bounding the plasma and r_p is a nominal plasma radius.

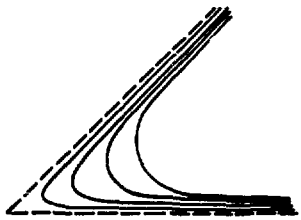

(a) Field lines in vacuum.

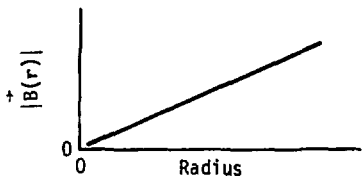

(b) Radial variation of magnetic field intensity in vacuum.

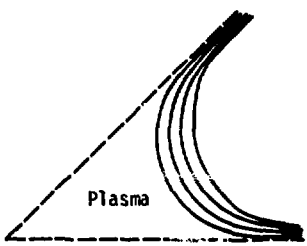

(c) Field lines in presence of high-beta plasma.

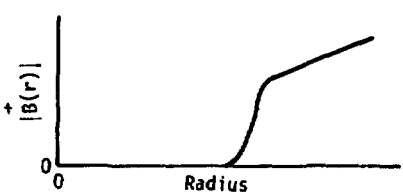

(d) Radial variation of magnetic field intensity with plasma present.

Fig. 7. Magnetic field in one octant of torus of Fig. 6.

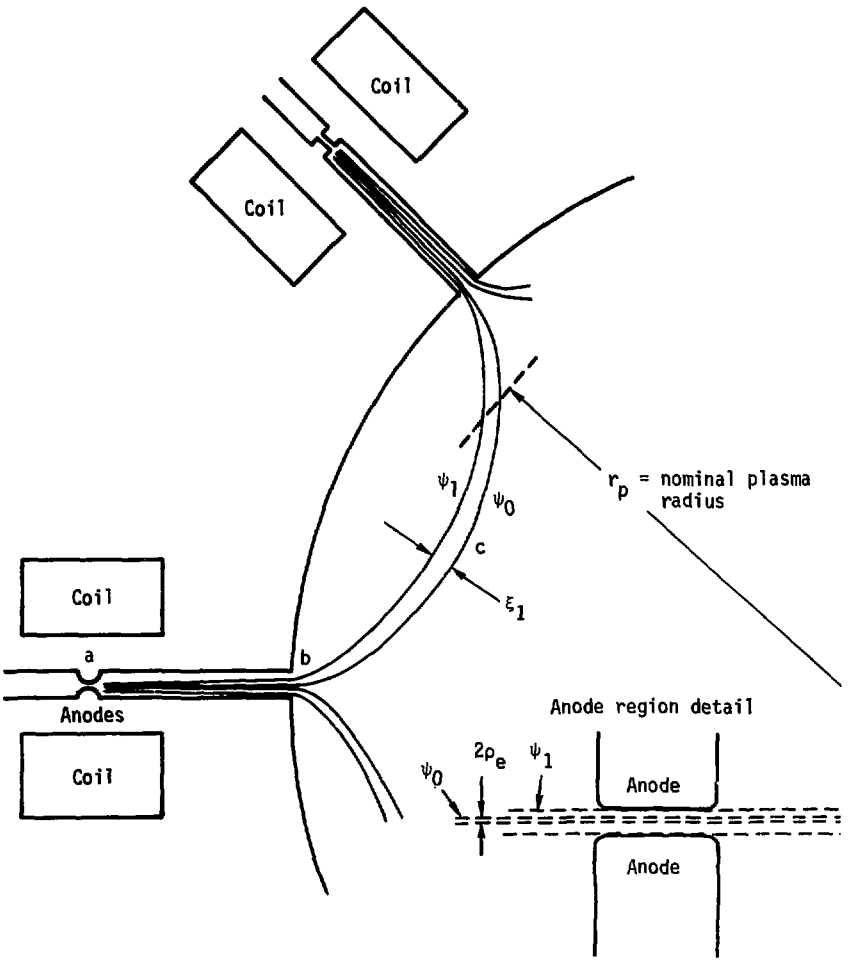

Fig. 8. Magnetic field lines along one segment of boundary, showing definitions of r_p, points a, b, c, flux surfaces ψ_0 and ψ_1, and distance ξ_1.

The diffusion coefficient is given by:

$$D = m_e T_e \nu_D / e^2 B^2 \ , \tag{7}$$

where the effective electron ion collision frequency for diffusion is[10]:

$$\nu_D = C_D n_e \ln \Lambda (1 + T_i/T_e)/T_e^{3/2} \tag{8}$$

where $C_D = 9.19 \times 10^{-17}$ m^3 $keV^{3/2}/s$, n_e is in m^{-3}, and T_e is in keV. The density gradient may be approximated as:

$$-\nabla n_e \simeq n_0/\xi_1 \ . \tag{9}$$

Using these equations in Eq. (4) we get:

$$\tau_d = \frac{\pi r_p^2 e^2}{m_e \int d\ell \ T_e \nu_D / \xi_1 B^2} \ . \tag{10}$$

Let ξ_0 and B_0 be the values of ξ_1 and B at any arbitrary reference point along the boundary. By magnetic flux conservation:

$$\xi_1 B = \xi_0 B_0 \ . \tag{11}$$

Because the central plasma is field-free and uniform, ν_D and T_e are constant along the boundary from b to c (Fig. 8). We will assume that they also have the same value from a to b. By definition, let $d\ell' \equiv d\ell/2\pi r_p$ and $B' \equiv B/B_0$. Then Eq. (10) may be written:

$$\tau_d = \frac{e^2 B_0^2 \xi_0 r_p}{2 m_e T_e \nu_D \chi_D} \equiv \frac{\xi_0 r_p}{\rho_0^2 \nu_D \chi_D} \ , \tag{12}$$

where:

$$\chi_D \equiv 2N \left(\int_a^b d\ell'/B' + \int_b^c d\ell'/B' \right) \ , \tag{13}$$

ρ_0 is the electron Larmor radius at the reference point, and N is the number of cusps; there are 2N identical segments around the plasma boundary.

For the coil system of Fig. 6, we choose to evaluate ξ_0 and B_0 at the anodes (point a, Fig. 8). We assume that $B = B_1 \equiv [2\mu_0 nk(T_e + T_i)]^{1/2}$ along the plasma boundary from b to c, and that B has its vacuum field values between a and b. Then:

$$2N\int_b^c d\ell'/B' \approx B_0/B_1 \quad . \tag{14}$$

The vacuum $\int_a^b d\ell/B$ is found by the computer program MAFCO,[11] with the result $\chi_D = 10.4$ for $B_0 = 8$ T, $B_1 = 1.23$ T. This value of χ_D, calculated for the N = 8 case, will also be used for the N = 6 case.

For a numerical example, we take $T_i = 20$ keV, $T_e = 30$ keV, $B_0 = 8.0$ T, $\xi_0 = 1.5$ mm, $n_e = 7.5 \times 10^{19}$ m^{-3}, and $r_p = 4.6$ m. For these values, we find that $\rho_0 = 7.31 \times 10^{-5}$ m, $\ln(\Lambda) \approx 18.8$, $\nu_D = 1320$ s^{-1}, and $\tau_d = 94$ s.

Several effects can reduce τ_d below this value: (1) on the inside of the torus (at small R) ξ_1 will be smaller than the value given by Eq. (11), due to the effect of toroidal curvature. This effect is partially compensated for by the fact that around the outside of the torus (at large R) ξ_1 will be larger than the value of Eq. (11). If desired, the magnetic field in the inner cusps can be increased at a small additional cost, since those coils have comparatively small radii.

(2) The value of ν_D may be increased above the value of Eq. (8) by anomalous effects, by cold plasma at the boundary, and by incident neutrals. Experiments involving plasma confinement in large multipole cusp chambers indicate that the level of turbulence in such systems is very low.[12] The sheath electric field and associated plasma drifts enhance the diffusion rate of cold electrons trapped in the anode regions, where strong diocotron oscillations occur,[13] but apparently do not hinder confinement of hot electrons, which pass through the anodes in a time that is short compared to the inverse growth rate of the oscillations.

To be pessimistic, we will ignore the "magnetic trapping time" mentioned earlier. Because τ_d is inversely proportional to n_e (via ν_D), it is convenient to define a function g_d such that:

$$\tau_d \equiv \frac{1}{n_e g_d(P, T_e, T_i)} \quad . \tag{15}$$

Then the loss rate from diffusion may be written:

$$(dn_e/dt)_{diff.} = -n_e^2 g_d \ , \tag{16}$$

which will be used in the conservation equations.

The energy loss rate from electronic heat conduction may be treated similarly. By definition, let:

$$\tau_{cond} \equiv \frac{\text{total thermal energy of electrons}}{\text{power loss by electronic heat conduction}}$$

$$= \frac{1.5 \int dV \, n_e T_e}{\int d\vec{S} \cdot (\kappa_{1e} \vec{\nabla} T_e)} \ . \tag{17}$$

If we use the approximate relation $\kappa_{1e} \approx nkD$, the result is:

$$\tau_{cond} = 1.5 \, \tau_d \ . \tag{18}$$

Boundary Layer

The boundary layer surrounding the plasma is illustrated in Fig. 9. For the final plasma parameters, $B_1 = 1.16$ T, $B_0 = 8$ T, and $\xi_0 = 1.5$ mm. From Eq. (11) it is found that the boundary layer thickness, $\xi_1 \approx 10$ mm.

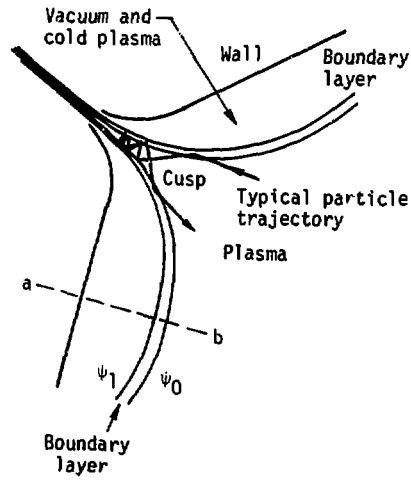

Fig. 9. Boundary layer between plasma and vacuum regions, bounded by flux surfaces ψ_0 and ψ_1.

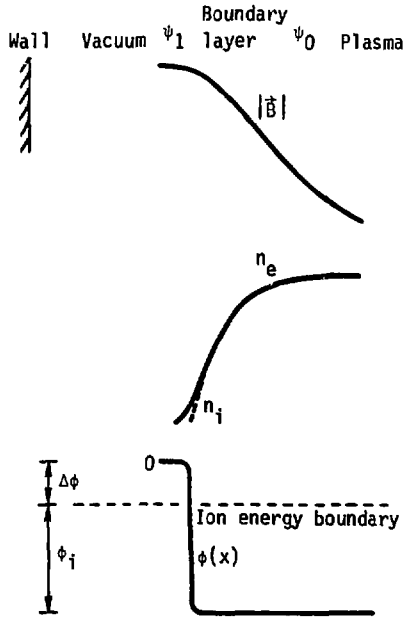

Fig. 10. Variation of magnetic field strength, B, electron density, n_e, ion density, n_i, and electrostatic potential in boundary layer.

The expected variation of parameters in the boundary layer is shown in Fig. 10. The magnetic field is gradually decreased to zero inside the plasma by diamagnetism. Electrons must diffuse across the magnetic field, but the ion Larmor radius (~2.4 cm) is larger than the boundary layer thickness; therefore, the ions are reflected primarily by the electrostatic barrier at the outside of the boundary region. This plasma sheath at ψ_1 will have a thickness of a few Debye lengths (λ_D = 0.09 mm). The quanitative sheath structure remains to be calculated.

Neutral atoms incident on the boundary layer have a mean free path, λ_m, given by:

$$\lambda_m \simeq \frac{v_m}{n_e(\langle\sigma_e v_e\rangle + \langle\sigma_i v_i\rangle + \langle\sigma_x v_i\rangle)} \quad , \tag{19}$$

where v_m is the average speed of the neutrals, n_e is the plasma density, and the reaction rates are for ionization by electrons, ionization by ions, and charge exchange. Ions produced by ionization along the potential slope are

accelerated inwards into the plasma. Assuming an exponential variation of potential in the sheath, Lavrent'ev found the average kinetic energy of these accelerated ions to be[7]:

$$W_1 = \frac{\lambda_D \phi_i}{\lambda_D + \lambda_m} . \qquad (20)$$

For a reactor plasma, $\lambda_m \sim 3\lambda_D$; so $W_1 \sim \phi_i/4$.

The fraction of incident neutral atoms that cause charge exchange is:

$$f_x \simeq \frac{\langle \sigma_x v_i \rangle}{\langle \sigma_e v_e \rangle + \langle \sigma_i v_i \rangle + \langle \sigma_x v_i \rangle} , \qquad (21)$$

and the fraction that become ionized is $f_1 \simeq 1 - f_x$. For molecular hydrogen incident on a proton-electron plasma, f_i ranges from about 0.28 at 10 keV to 0.4 at 20 keV.

Electrons produced by ionization along the potential slope are energetically unable to reach the plasma. They have orbits along magnetic field lines through the anode and back. Such electrostatically trapped electrons are to be distinguished from electrons that are trapped by the magnetic field in the boundary layer, and from those plasma electrons that are reflected by a "geometric mirror" effect of the converging magnetic field in the cusp gaps. The problem of finding the electron distribution function is complicated by the fact that there is no region of space to which all the electrons have access, due to these three competing trapping processes.

Magnetic mirror trapping and detrapping rates are well known from mirror confinement studies. The geometric mirror effect has been studied by Sidorkin and Lavrent'ev[6] and by Samec, Lee, and Fried.[14] We are interested in these processes mainly because they tend to decrease the density of electrons in the anode regions relative to the electron densities in the plasma and in the boundary layer. This decrease is beneficial, since a low electron density in the anodes results in a low value of $\Delta\phi$, a large value of ϕ_i, and good confinement of hot ions.

Electrostatic trapping of electrons, on the other hand, has the opposite effect: it tends to cause an accumulation of cold electrons in the anode regions, and a buildup of electron density there. Unless the confinement time of these trapped electrons is short, $\Delta\phi$ will become too large for adequate ion confinement. In what follows, the phrase "trapped electrons" will refer to electrostatically trapped electrons in the anode regions.

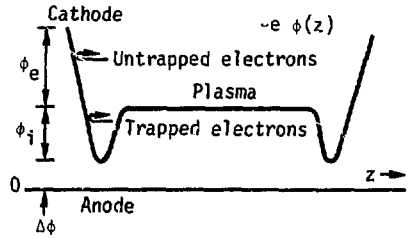

Fig. 11. Potential energy of electrons $-e\phi(z)$ vs position z along line through anodes.

Trapped Electrons

The potential energy of the electrons, $-e\phi(z)$, is found by turning Fig. 3 upside down, as illustrated in Fig. 11. Energetic electrons have access to both the plasma and anode regions, but cold electrons may be trapped in the potential well of the anodes and be unable to reach the main plasma. Trapped electrons are produced by the ionization of incident neutral gas and by the slowing down of plasma electrons via Coulomb collisions. The trapped electrons may be detrapped by collisional heating, lost by diffusion across the magnetic field, and lost by slowing down to low energies, where the cross-field diffusion rate is greatly enhanced by diocotron oscillations.

Let n_e be the plasma electron density, and n_u be the density of these untrapped electrons in the anode regions. Two effects act to reduce n_u below n_e: acceleration by the electric field, the geometric mirroring in the converging cusp plasma boundary. If the geometric mirroring effect is ignored, the ratio of n_u/n_e is given by[15]:

$$n_u/n_e = \exp(\phi_i/T_e)\ \mathrm{erfc}\left[(\phi_i/T_e)^{1/2}\right] . \qquad (22)$$

Let n_t be the density of trapped electrons in the anode region. The particle conservation equation for these electrons may be written in the form:

$$dn_t/dt = S_t + n_e/\tau_t - n_t/\tau_h - n_t/\tau_d' - n_t/\tau_L , \qquad (23)$$

where τ_t is the characteristic time for collisionally trapping untrapped electrons, τ_h is the time for untrapping trapped electrons by collisional heating, τ_d' is the trapped electron loss time by diffusion across the magnetic field, τ_L is the trapped electron loss time by cooling and enhanced diffusion, and S_t is the ionization source term.

The flux of neutral atoms incident on the plasma is $n_m v_m/4$, where n_m is the neutral density. The ionization source term is therefore:

$$S_t = S n_m v_m f_i / 4 V_1 \ , \tag{24}$$

where S is the surface area of the plasma, and V_1 is the volume along the boundary in which the ionization electrons are produced. Since $V_1 \simeq 3\lambda_m S$, Eq. (24) may be written:

$$S_t \simeq n_m v_m f_i / 12 \lambda_m \ . \tag{25}$$

The diffusion time of the trapped electrons across the short path λ_m is approximately:

$$\tau_d' \simeq (\lambda_m/\rho_t)^2/(\nu_D + \nu_{em}) \ , \tag{26}$$

where ρ_t is the trapped-electron Larmor radius, ν_{em} is the electron-neutral collision frequency for momentum transfer, and ν_D is the electron-ion collision frequency, which will be negligible for trapped electrons because of the paucity of ions in the trapped-electron region of the potential profile. The value of ν_{em} for molecular hydrogen is given approximately by:

$$\nu_{em} \simeq g_{em} n_m \ , \tag{27}$$

where:

$$g_{em} = 1.7 \times 10^{-3} \ (m^3/s).$$

The heating time and cooling time of trapped electrons will be roughly equal to the electron self-collision time given by Spitzer[16]:

$$\tau_h \simeq \tau_L \simeq \tau_{ee} \equiv C_{ee} T_e^{3/2}/(n_t + n_u) \ , \tag{28}$$

where $C_{ee} = 5.25 \times 10^{14} \ m^{-3} \ sec^{-1} keV^{-3/2}$ and we have taken the Coulomb logarithm $\ln\Lambda = 20$.

The trapping time for hot electrons is:

$$\tau_t \approx \frac{\text{total number of hot electrons}}{\text{number trapped per sec}}$$

$$= \frac{n_e V}{\int dV\, n_u/\tau_{ee}} = \frac{n_e V \tau_{ee}}{n_u V_t} \quad , \tag{29}$$

where V is the plasma volume and V_t is the volume of the region where untrapped electrons may be collisionally trapped, and the integration is over the volume where the trapping occurs. The situation is illustrated in Fig. 12.

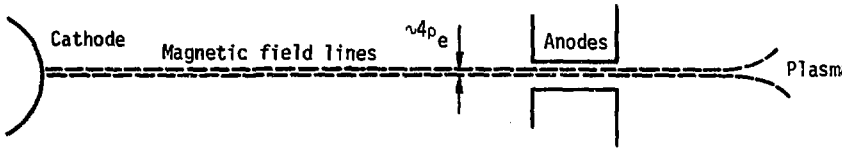

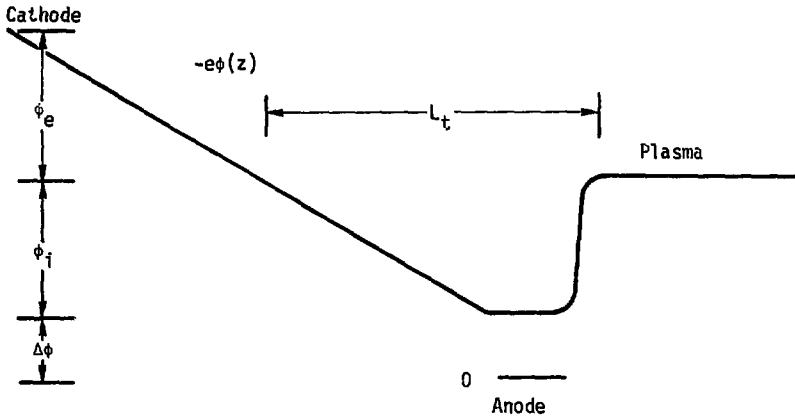

Fig. 12. Region in which untrapped electrons may be collisionally trapped, and electron potential energy, $-e\phi(z)$, in that region.

The width of the untrapped electron stream is roughly $4\rho_e$, and the length over which trapping can occur is L_t; therefore:

$$V_t \simeq 4\rho_e L_t 2\pi R\, N\ , \tag{30}$$

where ρ_e is the average Larmor radius of untrapped electrons, N is the number of cusps, and $2\pi R$ is the average circumference of the anode regions. The plasma volume is:

$$V = 2\pi^2 r_p^2 R_p\ , \tag{31}$$

where r_p and R_p are the minor and major plasma radii. Since $R_p \simeq R$, the trapping time may be written:

$$\tau_t \simeq \frac{\pi r_p^2 n_e \tau_{ee}}{4\rho_e L_t n_u N} \ggg \tau_{ee}\ . \tag{32}$$

Using Eqs. (24) through (29), Eq. (23) may now be written:

$$\frac{dn_t}{dt} = \frac{n_m v_m f_i}{12\lambda_m} + \frac{4n_u(n_t + n_u)\rho_e L_t N}{C_{ee} T_e^{3/2} \pi r_p^2} - \frac{2n_t(n_t + n_u)}{C_{ee} T_e^{3/2}}$$

$$- n_t g_{em} n_m (\rho_t/\lambda_m)^2\ . \tag{33}$$

The term containing the factor $\rho_e L_t / r_p^2$ is negligibly small compared to the other terms, and may be discarded. Let $x_t \equiv n_t/n_u$. At equilibrium, Eq. (33) may be written in the quadratic form:

$$\left(\frac{2n_u^2}{C_{ee} T_e^{3/2}}\right) x_t^2 + \left(\frac{2n_u^2}{C_{ee} T_e^{3/2}} + \frac{n_m n_u g_{em} \rho_t^2}{\lambda_m^2}\right) x_t - \left(\frac{n_m v_m f_i}{12\lambda_m}\right) = 0. \tag{34}$$

For example, we will consider the following parameters: $p_m = 0.00013$ Pa (10^{-6} Torr), $T_m = 1000$ K, $n_e = 6 \times 10^{19}$ m^{-3}, $T_e = 30$ keV, $T_i = 20$ keV, B = 8 T, $n_u/n_e = 1/3$, and an average trapped electron perpendicular energy of 30 keV. For these parameters, $n_m = 1.87 \times 10^{16}$ m^{-3}, v_m(D_2 molecules)

= 2030 m/s, $\lambda_m = 1.75 \times 10^{-4}$ m, $\rho_e = \rho_t = 7.3 \times 10^{-5}$ m, and $f_i = 0.39$, and the solution of Eq. (34) is $x_t = 0.31$, which means that $n_t < n_u < n_e$, and $n_t << n_e$. The characteristic times for heating, cooling, and diffusion of trapped electrons are on the order of milliseconds. For numerical calculations in the next subsection, Conservation Equations, we will take $x_t = 0.3$.

The total electron density in the anode region is:

$$n_A = n_t + n_u = n_u(1 + x_t) \sim 1.3\, n_u, \tag{35}$$

and this is the density that determines $\Delta\phi$ via Eq. (2).

The loss rate of plasma electrons by trapping is:

$$(dn_e/dt)_t = -n_e/\tau_t \equiv -n_e^2 g_t, \tag{36}$$

where:

$$g_t \equiv (n_u/n)^2 \left(4\rho_e L_t N/\pi r_p^2\right) (1 + x_t) \; /C_{ee} T_e^{3/2} \quad . \tag{37}$$

If it is assumed that trapped electrons are lost by enhanced diffusion (from diocotron oscillations) when their parallel velocity is less than a given value (when $v_\parallel < v_L$), then the resulting velocity-space loss boundaries have the shape illustrated in Fig. 13. Electrons are lost to the cathodes when their energy $1/2\ mv^2 > \phi_e$. Electrons from the guns start out with $v_\perp = 0$, $v_\parallel = v_c$; and electrons produced by ionization start out with $v_\perp = 0$, and $v_L < v_\parallel < v_t$, where $1/2\ mv_t^2 = \phi_i$. Electron trapping rates and distribution functions for these loss boundaries are being predicted by studying the random walk in velocity space of a large number of individual electrons and then averaging the results (the Monte Carlo technique).

Conservation Equations

The zero-dimensional conservation equations for particles and energy can be used to study plasma buildup and equilibrium parameters. Here we will use them to find equilibrium densities, temperatures, and potentials, with the goal of estimating Q, the power gain ratio, for a plasma sustained solely by electron beams from the cathodes. The seven unknowns to be found are n_e, n_i (the fuel ion density), n_A, T_e, T_i, ϕ_e, and ϕ_i.

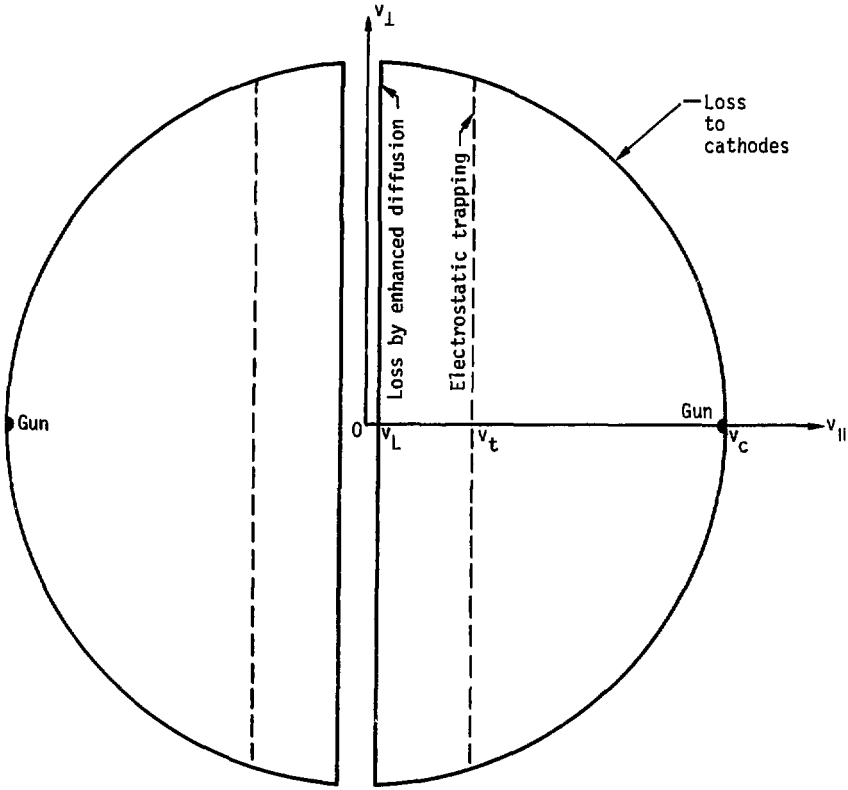

Fig. 13. Loss boundaries and trapping boundary for Monte Carlo simulation of electron velocity-diffusion.

We have considered the trapped electron density in the preceding subsection, because it is both a source and a sink for plasma electrons. A certain fraction of the electrons produced by ionization becomes detrapped by heating and joins the plasma. This fraction is approximately given by the equation:

$$\alpha_h = \frac{\tau_h^{-1}}{\left(\tau_h^{-1} + \tau_L^{-1} + \tau_d'^{-1}\right)} \quad . \tag{38}$$

Numerical estimates give $\alpha_h \sim 0.2 - 0.4$. In what follows we will assume a constant value $\alpha_h = 0.3$.

The particle conservation equation for plasma electrons may be written:

$$dn_e/dt = S_b + \alpha_h f_i S_m - n_e^2 (g_d + g_t) \quad , \tag{39}$$

where:

$$S_b \equiv (I_t/eV - n_e \nu_{ve}) \quad . \tag{40}$$

Here I_t represents the total current injected from the cathodes, and ν_{ve} represents the loss frequency of electrons back to the cathodes as they diffuse in velocity space over their potential barrier, ϕ_e,[5] so $I_e = eVS_b$ represents the net electron current that must be supplied by the cathode power supply. The influx of neutrals per unit volume per unit time is given by:

$$S_m = n_m v_m S/4V \simeq n_m v_m/2r_p \quad . \tag{41}$$

The quantities g_d, $f_i = 1 - f_x$, and g_t were defined in Eqs. (15), (21), and (37), and they represent loss by diffusion, fraction of incident neutrals undergoing ionization, and loss by trapping.

The conservation equation for ions may be written:

$$dn_i/dt = f_i S_m - n_i^2 (g_i + g_f) \quad , \tag{42}$$

where:

$$g_f = \langle \sigma v \rangle_{DT}/2 \quad , \tag{43}$$

$$g_i = C_{ew} \ln\Lambda \, (m_e/m_i)^{1/2} \left[2(\phi_i/\pi T_i)^{1/2} \exp(-\phi_i T_i) + \operatorname{erfc}(\phi_i/T_i)^{1/2} \right] / \phi_i^{3/2} \quad , \tag{44}$$

where $C_{ew} = 2.45 \times 10^{-16}$ keV$^{3/2}$m^3 s^{-1}, $\ln\Lambda$ is the Coulomb logarithm, $\langle \sigma v \rangle_{DT}$ is the D-T fusion reaction rate parameter, and we take m_i equal to 2.5 proton masses. The terms in Eq. (42) represent ion production by ionization, ion loss by velocity-diffusion over the potential barrier, ϕ_i,[5] and ion loss by fusion reactions. Recombination is negligible.

The sum of $\phi_e + \phi_i + \Delta\phi$ must equal the applied voltage, ϕ_A, as can be seen from Fig. 3. When Eq. (3) is used, this may be written:

$$\phi_e = \phi_A - \phi_i - \frac{\pi n_A e \rho_e x_2}{2\epsilon_0} \left[1 - \frac{2\rho_e}{\pi x_2} \ln (x_2/\rho_e) \right] . \quad (45)$$

From Eqs. (22) and (35), the anode electron density is found to be:

$$n_A = 1.3 n_e \exp (\phi_i/T_e) \operatorname{erfc} (\phi_i/T_e)^{1/2} . \quad (46)$$

The energy balance equation for electrons is similar to that used in Ref. 17, omitting terms for rf heating, alpha particle heating, and cyclotron radiation, and adding a term for heat conduction (combined with the g_d term):

$$1.5 d(n_e T_e)/dt = S_b \phi_e - 2.5 n_e^2 g_d T_e$$
$$- 1.5 C_{eq} \ln\Lambda \, n_e n_i \, (T_e - T_i)/T_e^{3/2}$$
$$- 1.5 C_{eq} \ln\Lambda \, n_e n_i f_k Z_k^2 (m_i/m_k)(T_e - T_i)/T_e^{3/2}$$
$$- Z_{eff} C_{br} n_e^2 T_e^{1/2} . \quad (47)$$

In this equation the potentials and energies are expressed in keV, f_k and Z_k are the fraction and atomic charge state of impurity species k (assumed to be at the same temperature as the fuel ions), m_k is the mass of the impurity, $Z_{eff} = \left(1 + f_k Z_k^2\right) / \left(1 + f_k Z_k\right)$, and impurity terms are summed over species k. The equipartition and bremsstrahlung coefficients have the values $C_{eq} = 4.01 \times 10^{-20}$ $m^3 keV^{3/2} s^{-1}$, $C_{br} = 3.4 \times 10^{-21}$ $m^3 keV^{1/2} s^{-1}$. We assume moderately light impurities that are fully stripped, and ignore line radiation and recombination radiation. The energy lost by electrons in ionizing collisions was estimated and found to be negligible in comparison with other terms. There is no term for trapping losses, because electrons carry away zero kinetic energy from the plasma when they become trapped.

The energy balance equation for the ions is:

$$1.5 d(n_i T_i)/dt = 1.5 C_{eq} \ln\Lambda \, n_e n_i (T_e - T_i)/T_e^{3/2} + f_i S_m \alpha_i \phi_i$$
$$- 1.5 f_x S_m T_i - n_i^2 g_i \phi_i - 3 n_i^2 g_f T_i , \quad (48)$$

where $\alpha_i = \lambda_d/(\lambda_d + \lambda_m)$ — see Eq. (20). The terms represent heating by electrons, acceleration of ions by the potential hill, charge exchange, velocity-diffusion losses, and loss of ions by fusion. It is assumed that the average energy of ions causing fusion is $3T_i$, which is the median energy of ions producing fusion reactions at $T_i = 10$ keV.[18]

Because departure from charge neutrality occurs only in a thin sheath around the edges, the quasineutrality condition may be applied:

$$n_e = n_i(1 + f_k Z_k) \quad . \tag{49}$$

We have ignored alpha particle density and heating effects, because the alpha particle confinement time is very short.

Equations (38) through (49) constitute a complete set of conservation equations and auxiliary equations for finding the seven unknowns as a function of time for any given initial conditions.

The equilibrium solutions of this set of nonlinear equations have been found by three different methods. First, all variables except for T_e, T_i, and ϕ_i are eliminated algebraically. The first method starts with assumed values of these variables and solves each of the three equations iteratively for one of the variables, using the most recent values of all three variables. If the initial values are adroitly chosen, the values of the three unknowns converge to the correct solution after many cycles of solving the three equations iteratively. This method requires very little computer time, but converges only rarely.

The second method is to integrate the ordinary differential equations for dn_e/dt, $d(n_iT_i)/dt$, and $d(n_eT_e)/dt$ in time from some assumed initial values, until equilibrium is reached. At each time step the value of ϕ_i is found iteratively from Eqs. (39), (42), and (49). This method converges more often than the first method, but the initial values of n_e, T_e, and T_i must still be chosen carefully to avoid divergence, because of the nonlinearity of the equations for ϕ_i.

The third method is to evaluate the residuals R_1, R_2, and R_3 of the three equations for T_e, T_i, and ϕ_i for many combinations of these variables, and to search for the minimum of the sum $\left(R_1^2 + R_2^2 + R_3^2\right)$.[19] By dividing the volume searched into finer and finer increments, any desired degree of accuracy can be obtained. This method almost always gives the correct solution of the equations, and it has been checked with solutions from the first two

methods for cases in which they converged. Although it consumes much more computer time than the other two methods, this method was used for most of the computations because of its reliability in converging.

The values of fusion cross sections and atomic collision cross sections are computed by subroutines using empirical formulas[20] and polynomial approximations.[21]

In calculating the power gain ratio, Q, we assume that a fraction f_c of the escaping ions is collected at an ion collector at potential $-\Delta\phi$, and the remainder $(1 - f_c)$ is collected at the cathode voltage, ϕ_A. The power gain ratio may be written:

$$Q = \frac{0.25 n_i^2 \langle\sigma v\rangle_{DT} W_f}{S_b \phi_A + n_i^2 g_i \left[f_c \Delta\phi + (1 - f_c)\, \phi_A \right]} , \qquad (50)$$

where W_f = 17 600 keV, and the terms in the denominator represent power inputs for electron currents from the cathode and ion currents to the cathode.

For the numerical calculations we take the following basic set of parameters: B = 8 T, r_p = 2.8 m, R_p = 9.5 m, an optimum neutral gas feed rate (see the first subhead under Operation), T_m = 1000 K, x_1 = 0.001 m, x_2 = 0.002 m, L_t = 1 m, N = 6 cusps, f_c = 0.95, ϕ_A = 300 kV, and a 1%

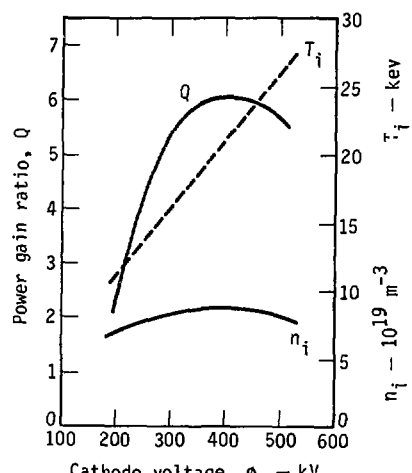

Fig. 14. Variation of fuel ion density, n_i, ion temperature, T_i, and power gain ratio, Q, with applied voltage, ϕ_A, for N = 6 toroidal multipole cusp (parameters described in Magnet Coils section under Coil Selection) with magnetic field, B = 8.0 T, and electron beam injection current of 1.0 A/m^3, assuming a 1% aluminum impurity and the optimum neutral gas feed rate (Operation section, under Gas Feed Rate).

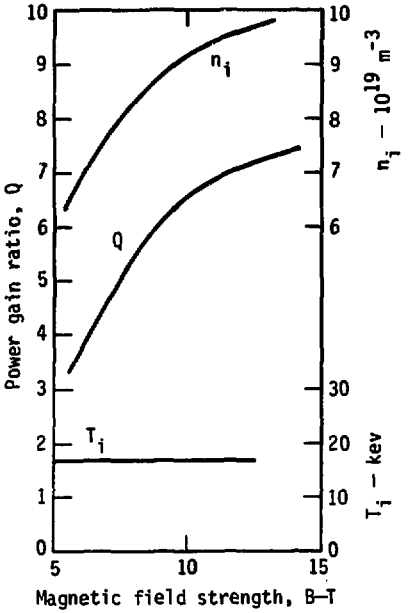

Fig. 15. Variation of n_i, T_i, and Q with magnetic field, B, for the same case as Fig. 14, with applied voltage = 300 kV.

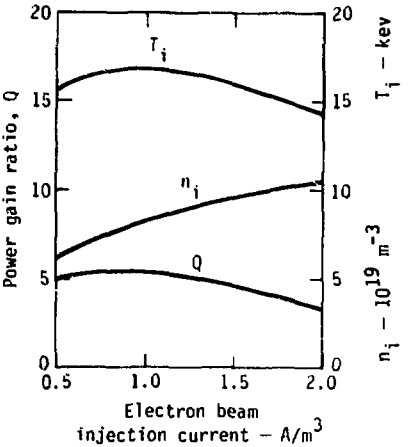

Fig. 16. Variation of n_i, T_i, and Q with electron beam injection current per unit volume, for the case of Fig. 15 with B = 8 T.

aluminum impurity (f_k = 0.01, Z_k = 13, m_k/m_i = 27/2.5). For this impurity, $n_i = 0.89n_e$, and Z_{eff} = 2.39.

The resulting values of n_i, T_i, and Q found from the equilibrium solution of the conservation equations are shown in Fig. 14 as a function of ϕ_A. The variation of these parameters with B is shown in Fig. 15, and the variation with electron beam injection current is shown in Fig. 16.

Satisfactory Q values are obtained for applied voltages over 250 kV. The ion temperature rises almost linearly with voltage, but depends little on magnetic field. The value of Q begins to drop at high voltage because each ampere of current used to sustain the plasma density requires more input power than at lower voltages.

Magnet Coils

Design Criterion

The coil system is designed to maximize the ratio of fusion power output to coil cost. This ratio may be written:

$$\frac{0.25 n_i^2 \langle \sigma v \rangle_{DT} W_f V}{K V_c} ,$$

where W_f = 17.6 MeV, V = plasma volume, V_c = coil volume, and K is the coil cost per unit volume.

For fixed magnetic field, B, and applied voltage, the density and the ion temperature are roughly constant, and the ratio of fusion power to coil cost is proportional to V/V_c. Therefore, the design criterion used here is to look for coil systems that achieve large values of V/V_c without requiring impractically large V_c.

For the purpose of comparing different systems, the plasma volume is taken to be the volume bounded by the magnetic isobar $|\vec{B}|$ = 1.5 T. This is approximately the region inside which the magnetic field is excluded by plasma diamagnetism for $n_e = 10^{20}$ m^{-3}, $T_e + T_i$ = 50 keV.

Cusp Geometries Available

Several cusp geometries are illustrated in Fig. 17. The spindle cusp, which consists of two circular coils with opposite currents, is unsuitable because of its small plasma volume. The toroidal set of ring cusps is effectively a bunch of spindle cusps connected end to end. It will also have a small plasma volume, unless the coils are placed close together. A small aspect ratio would be efficient in producing a large plasma volume, but the magnetic field would be quite weak on the outside compared with the field on the inside.

A spherical multipole cusp[9] is the best possible, since it has the highest ratio of volume to surface area. However, it is uncertain whether the point cusps on the axis can be effectively plugged at high plasma densities. We will be pessimistic in the present study and consider a system with only line cusps.

The toroidal multipole cusp, like the set of ring cusps, consists of only line cusps, and it probably will have a larger ratio V/V_c. Therefore,

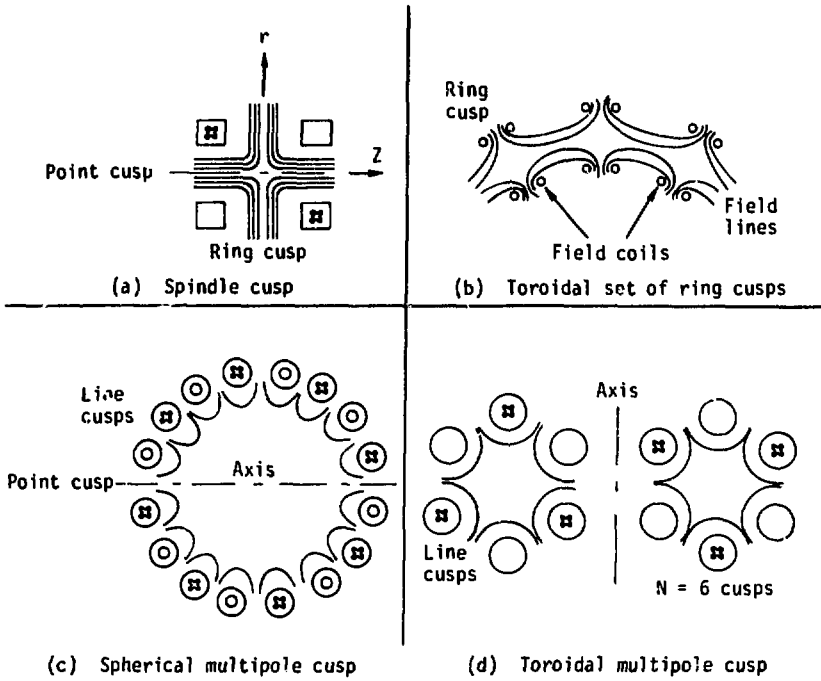

Fig. 17. Some magnetic cusp geometries that are suitable for electrostatic plugging.

toroidal multipole cusps are studied in detail in this work, to determine the maximum possible V/V_c. Because this choice has not been checked by calculating V/V_c for the toroidal set of ring cusps, it would be worthwhile to do that in the future.

Parameter Study of Toroidal Multipole Configuration

The geometry used for most of this study is a toroidal multipole configuration with N = 4, 6, 8, ... cusps, as illustrated in Fig. 18. Because the ratio V/V_c is roughly a ratio of volume to surface, it appears efficient to arrange the multipole coils around a circular chamber. A blanket plus shield thickness of 1.5 m is used between the plasma and the

coils. The parameters N, a_0, b, c, w, and h have been varied to study the consequent values of V_c and V/V_c. The current in each filament is fixed by assuming that $J = 2.5\ kA/cm^2$.

The first study assumes $a_0 = 5$ m, c = 3 m, and $B \geq 10$ T in all cusps. For given values of N, b, and w, h is adjusted to achieve the required magnetic field strength. The plasma shape is assumed to be elliptical in computing the volume V. The results of this study are listed in Table 1 and plotted in Fig. 19.

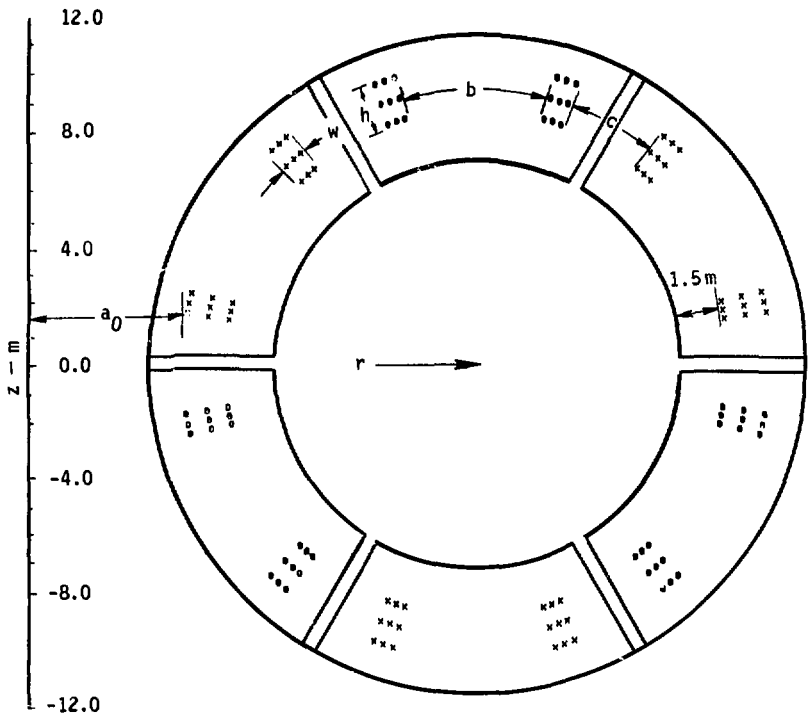

Fig. 18. Toroidal multipole configuration (number of cusps = 6); w = coil width; h = coil thickness in the direction of the minor radius, c = gap between opposed coils, b = gap between like coils, a_0 = distance from innermost coil to major axis of torus.

For each value of b there is a curve containing various combinations of w and h. The maximum ratio of V/V_c at any given coil volume is given approximately by the dashed curve tangent to this family of curves. Because points for N = 4 have very small V/V_c, this case is less economical. For N = 6 and N = 8, the curve rises very rapidly with coil volume, indicating that large systems will have a strong economic advantage, up to the limit imposed by wall loading and radiation damage considerations.

Because coil volumes, $V_c \sim 3000\ m^3$, are very large and expensive, a further study has been conducted to seek reasonable values of $V/V_c \geq 1$ at smaller $V_c \sim 1000\ m^3$. Three parameter changes are made to explore the lower volume regime: a_0 is reduced to 3 m, c is reduced to 2 m, and B is reduced to 8 T. The results of this parameter study are listed in Table 2 and plotted in Fig. 20. These plasma volumes are calculated assuming the plasma cross section to be circular.

There is again a steep increase of V/V_c with b, as in the previous case. The maximum attainable value of b is limited to about 3 m at B = 8 T, however. At larger values of B the 1.5-T isobar bulges out into the chamber walls, spoiling confinement. Somewhat larger values of b are attainable at higher magnetic fields, because the 1.5-T isobar is pushed inwards slightly.

A typical plot of magnetic isobars is shown in Fig. 21. For this case the plasma boundary will lie between the first and second contours.

With a_0, b, c, and h held constant, an increase of magnetic field strength (by increasing w) strongly decreases the attainable value of V/V_c, as shown in Fig. 22.

The point labelled 4E in Fig. 20 is for a cusp with N = 4 and its axes rotated, as shown in Fig. 23. The additional weak coil at the center is needed to prevent the isobars from bulging inwards along the major radius.

Because elongating the circular multipole geometry vertically into an elliptical shape slightly increases V/V_c, a little can be gained from optimization in this regard.

Coil Selection

In order to minimize V_c, the parameters a_0 and c should be kept as small as feasible, which is about 2 and 3 m, respectively, allowing space for structural materials, high voltage feedthroughs, and coil shielding. Optimized designs may result in some reductions from these values.

Table 1. Summary of toroidal cusp volume calculations.

a_0 = 5 m, c = 3 m, B = 10 T, J = 2.5 kA/cm^2

N	b(m)	w(m)	V(m^3)	V_c(m^3)	V/V_c
4	3	1	116	1127	0.103
4	3	2	204	1481	0.138
4	3	3	337	1961	0.172
4	5	1	384	1345	0.285
4	5	2	648	1723	0.376
4	5	3	836	2241	0.373
6	1	1	718	1626	0.442
6	1	2	1416	2312	0.612
6	1	3	3034	3228	0.940
6	3	5	1100	2536	0.434
6	3	1	2093	2168	0.966
6	3	2	3879	2884	1.34
6	3	3	5590	3915	1.43
6	5	5	3094	3403	0.909
6	5	1	5399	2596	2.08
6	5	2	8452	3408	2.48
6	5	3	11709	4487	2.61
8	0	1	1029	1914	0.538
8	0	1.5	1236	1884	0.656
8	0	2	2086	2061	1.012
8	0	2.5	2610	2319	1.125
8	3	0.5	5668	3908	1.45
8	3	1	9344	3428	2.73
8	3	2	17168	4690	3.66
8	5	0.5	12608	4657	2.71
8	5	1	20939	4225	4.89
8	5	2	30321	5557	5.46

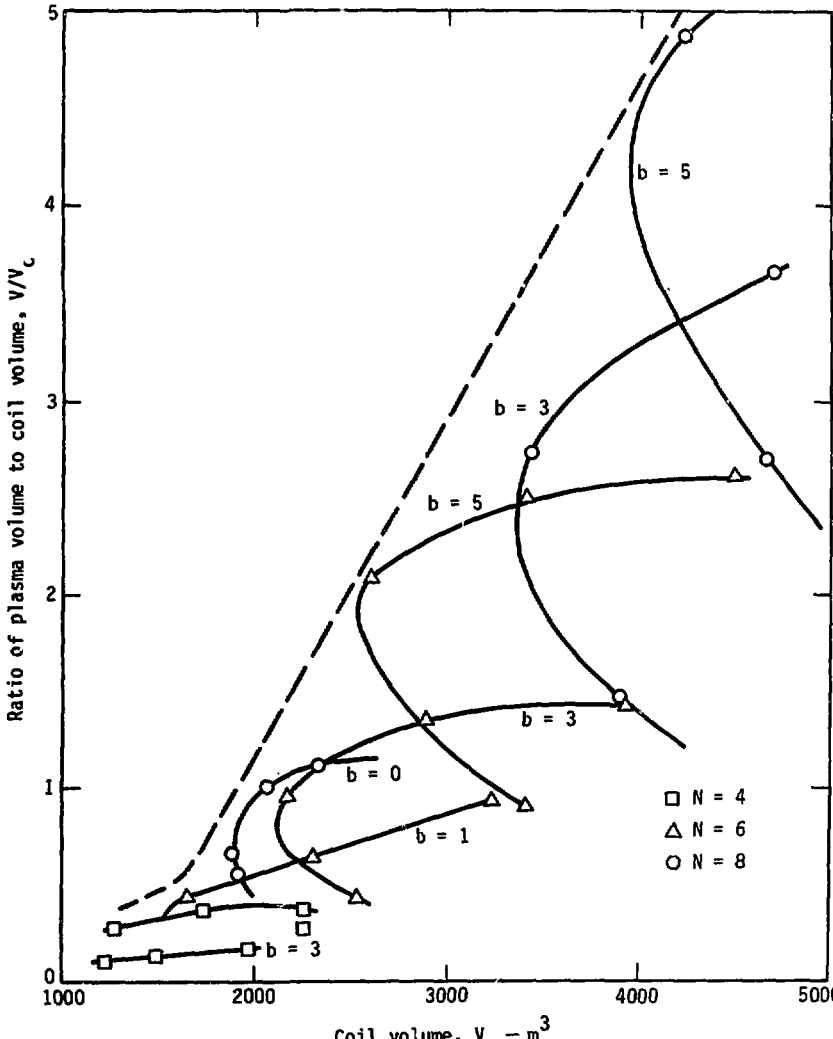

Fig. 19. Ratio of plasma volume to coil volume for toroidal multipole cusp coils as a function of coil volume, assuming B = 10 T, a_0 = 5 m, c = 3 m, J = 2.5 kA/cm^2.

Table 2. Toroidal cusp volume calculations.

a_0 = 3 m, c = 2 m, B = 8.0 T

	Major radius of plasma, R (m)	Minor radius of plasma, r_p (m)	Plasma volume, V (m^3)	Coil volume, V_c (m^3)	Ratio of V/V_c
6B10H10W14[a]	8.39	2.18	789.	871.	0.906
6B20H10W16	9.44	3.00	1682.	1092.	1.541
6B30H10W16	10.43	3.88	3093.	1291.	2.397
6B40H10W16	11.39	4.80	5172.	1470.	3.518
6B10H20W06	7.96	1.67	449.	639.	0.702
6B20H20W06	8.60	2.04	705.	795.	0.887
6B30H20W07	9.52	2.82	1498.	935.	1.603
6B40H20W07	10.44	3.69	2799.	1062.	2.635
6B10H30W05	7.94	1.08	183.	725.	0.252
6B20H30W05	8.87	1.71	509.	892.	0.571
6B30H30W05	9.78	2.43	1139.	1040.	1.096
6B40H30W05	10.68	3.24	2214.	1176.	1.882
8B10H10W14	10.21	3.92	3100.	1423.	2.178
8B20H10W16	11.69	5.20	6245.	1812.	3.446
8B30H10W16	13.06	6.49	10869.	2156.	5.043
8B10H20W06	8.95	2.55	1151.	1001.	1.150
8B20H20W06	10.25	3.63	2666.	1262.	2.113
8B30H20W07	11.53	4.80	5248.	1503.	3.491
8B40H20W07	12.80	6.04	9204.	1725.	5.336
8B10H30W05	9.14	2.12	814.	1112.	0.732
8B20H30W05	10.42	3.13	2019.	1391.	1.452
8B30H30W05[b]	11.67	4.25	4161.	1643.	2.533
8B40H30W05	12.92	5.44	7536.	1878.	4.013

[a]See footnote b.

[b]8B30H30W05 means N = 8, b = 3.0 m, h = 3.0 m, w ≤ 0.5 m.

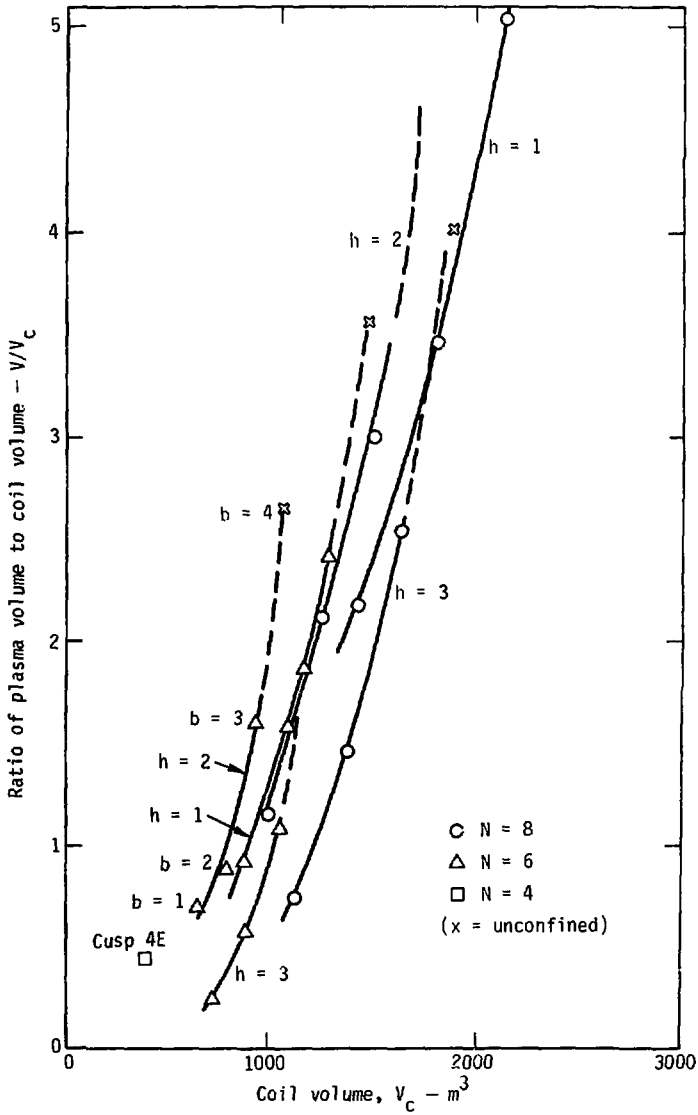

Fig. 20. Ratio of plasma volume to coil volume for toroidal multipole cusp coils as a function of coil volume, assuming B = 8 T, a_0 = 3 m, c = 2 m, J = 2.5 kA/cm^2.

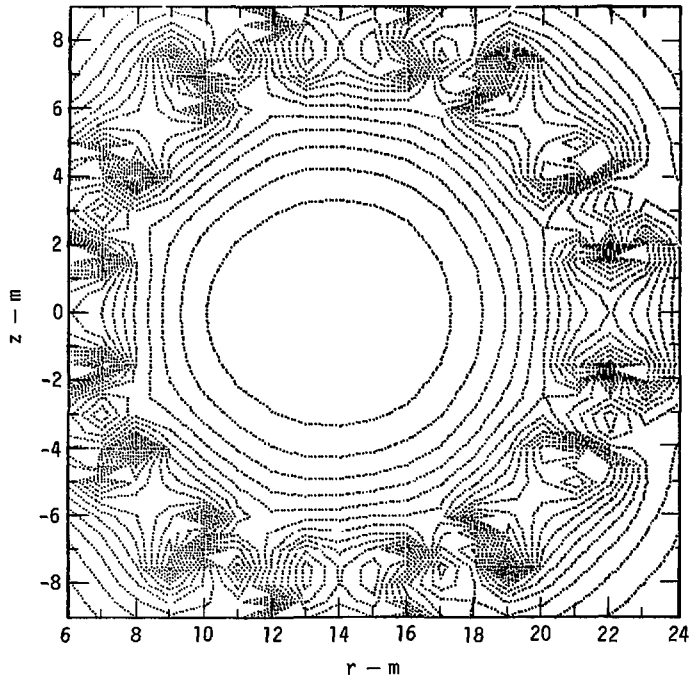

Fig. 21. Typical plot of constant $|\vec{B}|$ contours of the vacuum magnetic field for the case N = 8, b = 2 m, h = 2 m, w = 0.7 m (B = 8 T in all cusps; contours are at 0.83 T, 1.65 T, 2.47 T, . . .).

Only values of h = 1, 2, and 3 m have been studied here. The best results are obtained with h = 2 m.

Because the magnetic field is about 10% stronger in the cusps around the outside of the torus, the coils there can be reduced in size to equalize B in all the cusps. This reduction will result in about a 5% decrease in V_c.

The value of V/V_c rises very steeply with b; therefore, the maximum value of b consistent with good confinement should be chosen. This choice is made by drawing in the shield and making sure that the plasma boundary does not touch the chamber walls. When B = 8 T, the maximum value of b is approximately 3 m, for the N = 6 and N = 8 cases.

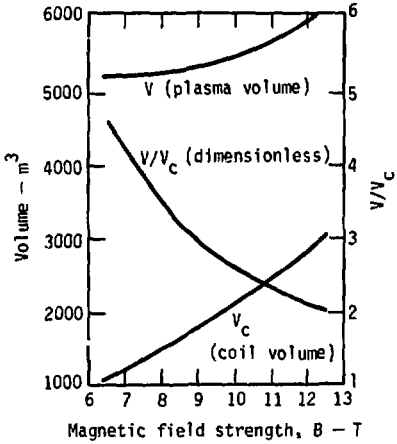

Fig. 22. Variation of coil volume, plasma volume, and V/V_c as B is increased by increasing coil width w, for N = 8, b = 3 m, h = 2 m.

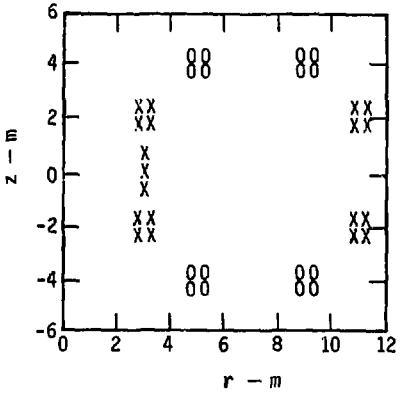

Fig. 23. Coil geometry for Cusp 4E.

The minimum value of V_c required to confine a given plasma volume is summarized in Fig. 24. For small plasma volumes ($\sim$200 m^3) the coil configuration of Cusp 4E is best. For intermediate volumes ($\sim$1000 m^3) the cusps with N = 6, h = 2 are best, and for large plasma volumes ($\sim$4000 m^3) coils with N = 8, b = 3, h = 2 are desirable. For comparison, coil systems planned for the mirror hybrid fusion-fission reactor,[22] the mirror reactor,[23] the PPL-Tokamak reactor,[24] and the UWMAK-II reactor[25] are indicated on the graph.

From the standpoint of improving plasma confinement, it is highly desirable to use the maximum value of N,[6] which might make it ultimately desirable to use configurations with larger N and smaller b, such as b = 0, N = 16. However, because this aspect of the confinement theory is not yet thoroughly developed, the selection here is based primarily on minimizing V_c.

If point cusps can be effectively plugged, then a spherical plasma volume will be possible, with an even better ratio of V/V_c than those in Fig. 24.

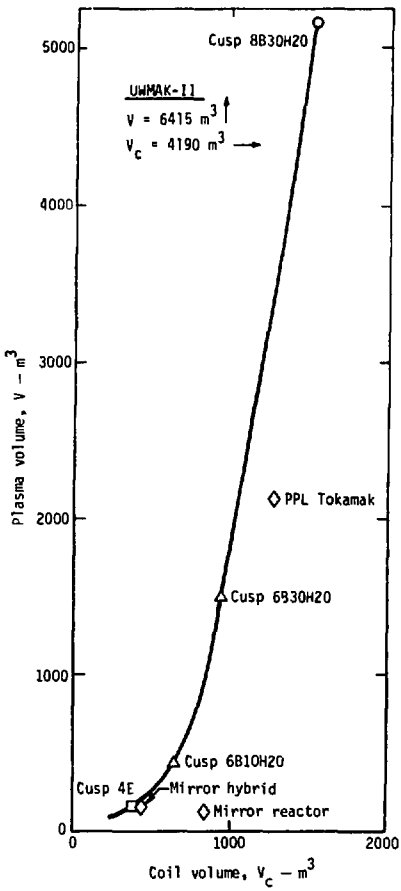

Fig. 24. Plasma volume vs coil volume for toroidal multipole cusp coils with B = 8 T.

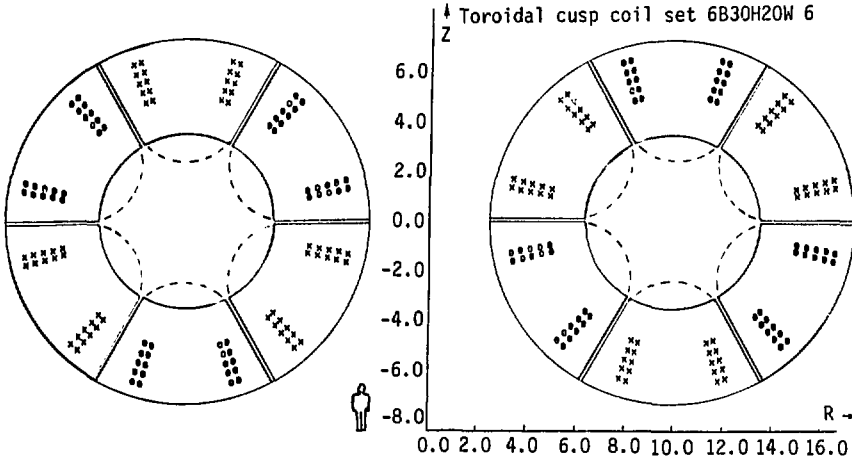

Fig. 25. Toroidal coil configuration with N = 6, b = 3 m, h = 2 m, a_0 = 3 m, c = 2 m (major and minor radii of chamber are ∿10 and 3.6 m).

Because the coil efficiency, V/V_c, decreases markedly with increasing B (Fig. 22), there is a strong incentive for using the minimum value of B consistent with good confinement. The required B can be determined by choosing the wall power loading and then calculating the required plasma parameters to produce this wall loading.

In the present design the cusp configuration with N = 6, b = 3 m, h = 2 m, a_0 = 3 m, c = 2 m is chosen. The coil mass and length for this system are 6.85×10^6 kg and 2.3×10^{10} Am. The coils are shown in Fig. 25.

The plasma radii are estimated to be 9.5 and 2.8 m, with a wall radius of 3.6 m.

Structure

Coil Forces

Coil forces are calculated for a coil in the outermost cusp. This coil is split into 15 segments, as illustrated in Fig. 26. The magnetic field is

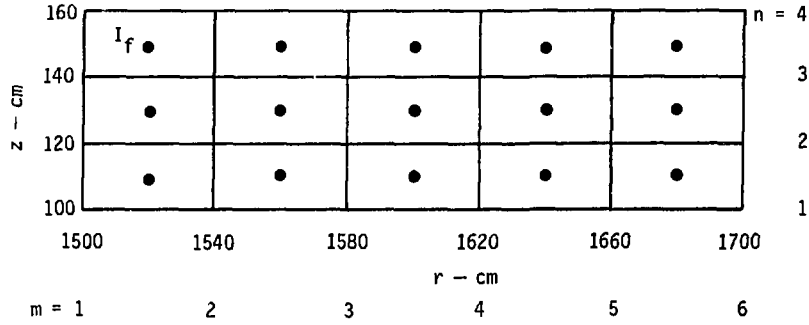

Fig. 26. Cross section of one of outer cusp coils, showing division into 15 segments for finding coil forces (dimension r is measured from major axis of torus, which is coil axis).

calculated at each corner of a segment, and the field at the conductor is taken to be the average of the four corner values. The total radial and axial forces per unit length of the coil are then found from the equations:

$$F_z/L = I_f \sum_m \sum_n \delta_{mn} B_{rmn}/4 \ , \tag{51}$$

$$F_r/L = -I_f \sum_m \sum_n \delta_{mn} B_{zmn}/4 \ , \tag{52}$$

where I_f is the current in one segment, B_{rmn} and B_{zmn} are the radial and axial field components at point (m,n) and

$$\delta_{mn} = \begin{cases} 1 & \text{for corner points} \\ 2 & \text{for edge points} \\ 4 & \text{for interior points.} \end{cases} \tag{53}$$

The resulting forces per unit length are found to be $F_z/L = 8.70 \times 10^7$ N/m and $F_r/L = 8.42 \times 10^6$ N/m.

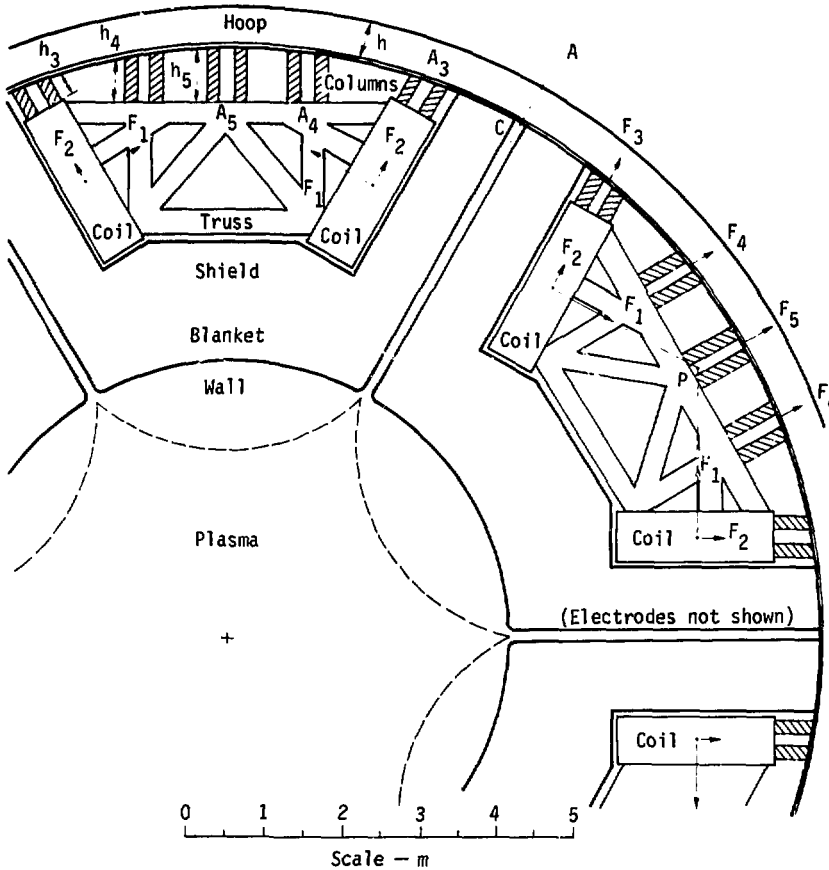

Fig. 27. Structure design, showing forces F_1 and F_2 calculated for coil at right and assumed to be same in other cusps. (If all coils had the same current, the magnetic field would be strongest in outer cusp.)

Structural Design

The structural design is shown in Fig. 27. The coil forces F_1 and F_2 are all assumed to be equal to the forces F_z/L and F_r/L found above. Each pair of coils is supported by a truss at coil temperature, which combines the F_1 forces of the two coils. The vector sum of these two F_1 forces at the

intersection of their lines of action (point P) is a force equal in magnitude to F_1 and directed radially outwards. The outward forces are transmitted by fiberglass columns to the hoop at room temperature. The force F_3 is approximately equal to F_2, and the sum of forces $(F_4 + F_5 + F_4)$ is approximately equal to F_1. With these approximations, the tension F_6 in the hoop at point A is found to be 1.03×10^8 N/m, and the bending moment at A is found to be approximately 1.9×10^8 Nm/m.

The hoops will cover one third of the reactor surface area, leaving the remaining two thirds for electron guns, ion collectors, vacuum pumping, etc. Then the force in the hoop is effectively $3F_6$. The strain of the hoop is found from the equation:

$$\varepsilon = 3F_6/hE \ , \tag{54}$$

where h is the height of the hoop and E is the modulus of elasticity. For steel, $E \simeq 2 \times 10^{11}$ N/m^2. If we take h = 0.5 m, the resulting strain is $\varepsilon = 0.0031$. For a hoop radius of 8 m, the elongation in radius is 2.5 cm.

The total hoop mass is found from the equation:

$$M_h = \rho f_s \left(4\pi^2 r_0 R\right) h \ , \tag{55}$$

where $\rho = 8000$ kg/m^3 is the density of the steel, $f_s = 1/3$ is the fraction of the surface area occupied by the hoops, R is the major radius of the torus (10 m), and $r_0 = 8$ m is the mean hoop radius. For the above parameters, the total hoop mass is $M_h = 4.2 \times 10^6$ kg.

The trusses have not been designed, but it is possible to make them quite rigid and still have a total mass less than the total hoop mass. With other minor structural masses the total structural mass will be about twice the total hoop mass, or 8.4×10^6 kg. This figure compares favorably with masses for mirror coil clamps.[26,27]

Columns

By definition, let $f_4 = F_4/F_1$. Then $F_5 = F_1(1 - 2f_4)$. In calculating the heat leak from the hoops along the fiberglass columns to the cryogenic truss and coils, the results will be insensitive to the value of f_4, since the lengths h_4 and h_5 of the columns supporting F_4 and F_5 are nearly equal. We will assume $f_4 = 0.2$. The heights of the columns are $h_3 = 0.5$ m,

$h_4 = 0.7$ m, and $h_5 = 0.8$ m. The design stress used for the glass-epoxy laminate NEMA G-10 is 7×10^7 N/m^2 (10^4 psi).[24] The required cross-sectional areas are found from the equations:

$$A_3 = F_2/f_s\sigma, \qquad A_4 = f_4F_1/f_s\sigma, \qquad A_5 = (1 - 2f_4)\ F_1/f_s\sigma, \qquad (56)$$

where σ is the design stress. For the above parameters, $A_3 = 0.746$ m^2/m, $A_4 = 2.24$ m^2/m, and $A_5 = 0.361$ m^2/m. The thermal conductivity of the fiberglass is $k_t = 0.26$ W/mK, so the resulting heat leak is found to be:

$$q = k_t N\ 2\pi R\ (2A_3/h_3 + 2A_4/h_4 + A_5/h_5)\ \Delta T = 181 \text{ kW},$$

for $\Delta T = 290$ K. This heat leak is unacceptably large. It will be reduced by lengthening the columns, up to the limit imposed by buckling. This lengthening will require moving the hoops out to a slightly larger radius. For example, if the column lengths could be roughly tripled, then q would be 60 kW, which is quite acceptable, and the hoop radius would increase by ~1.5 m. Another possible solution would be to have the hoops also at the coil temperature, but this would require more complex dewars and much longer cooldown times.

The other heat loads from conduction through the superinsulation and neutron heating have not been calculated.

Electrodes

Anodes

Most of the cusp gaps will have plugging electrodes, as illustrated in Fig. 28. Two collimators, each 0.6 m long and spaced 0.8 m apart, with a 1-cm gap collimate the primary radiation to a narrow beam with a divergence angle of 0.3 deg. The anodes, located just behind the second collimator, are 0.2 m wide with a 3-mm gap between them and a refractory metal tip.

The anodes are aligned as follows. A telescopic probe P is lowered into place behind the anodes with the magnet coil energized. An electron beam is injected into the plasma region from one of the other cusps. Some of the electrons will emerge out the cusp along the magnetic field plane of symmetry (dashed line) and be detected by the probe. The top anode is moved down

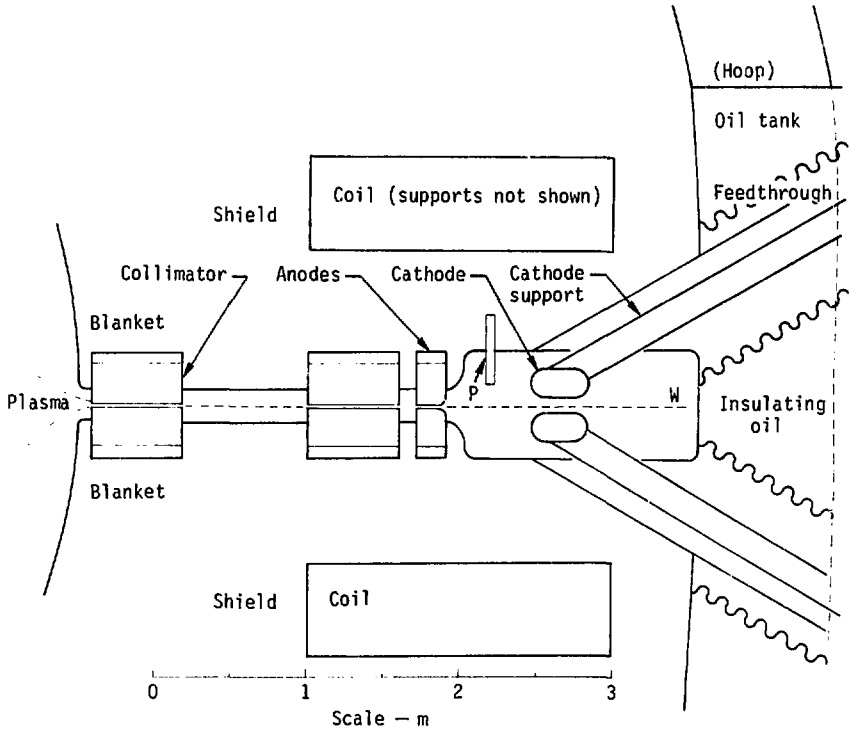

Fig. 28. Plugging electrodes in one of six cusps.

until the electron current is cut off, then moved back up, and a plot of probe current vs anode position is drawn. Then the process is repeated for the bottom anode. Because the width of the electron stream is only 0.15 mm, this method can be quite accurate. The anodes are then positioned so that each is 1.5 mm from the midplane, the probe is withdrawn, and the process is repeated for other segments of the same cusp, and for the other cusps. The anodes will contain multiple temperature gages to detect possible overheating during operation.

Because the anode supporting structure is not tied to the coils, the coil deflections will not act directly on the anodes, but indirectly, via the expansion of the hoops, calculated in the Structure section. However, during

operation, thermal stresses and other effects will tend to warp the anodes. The present design is based on the assumption that the anode spacing can be maintained at 3 mm ± 1 mm during operation. Thermal stresses have not been calculated.

All of the electronic heat loss from the plasma by diffusion and heat conduction is assumed to be deposited on the anodes, with additional energy gain as the electrons fall through the potential $(\phi_i + \Delta\phi)$. Thus, the power deposited on the anodes is:

$$P_A = n_e V(2.5T_e + \phi_i + \Delta\phi)/\tau_d \ , \tag{57}$$

where the terms on the right were defined in the Theory section.

The number of trapped electrons produced per second that impinge on the anode is equal to:

$$(1 - \alpha_h)\ f_i n_n v_m S/4 \ , \tag{58}$$

and the average energy they acquire as they fall into the anode is approximately $(\phi_i/2 + \Delta\phi)$. Thus, the heat load on the anode from trapped electrons is:

$$P_{At} = (1 - \alpha_h)\ f_i n_m v_m S\ (\phi_i/2 + \Delta\phi)/4 \ . \tag{59}$$

For typical operating parameters, $n = 10^{20}\ m^{-3}$, $T_e = 17$ keV, $\phi_i = 140$ keV, $\Delta\phi = 72$ kV, $V = 1470\ m^3$, $\tau_d = 19$ s, $n_m v_m/4 \approx 4.8 \times 10^{18}\ m^{-2}s^{-1}$, $S = 1050\ m^2$, $f_i = 0.3$, and $\alpha_h = 0.3$. The resulting powers deposited on the anode from plasma electrons and trapped electrons are found from Eqs. (57) and (59) to be 315 and 24 MW.

The total length of the anodes is:

$$L_A = 2N(2\pi R = 750\ m; \tag{60}$$

therefore, the heat deposited per unit length is 4.5 kW/cm. The anode detail is shown in Fig. 29. The leading edge of the anode is gradually tapered so that this heat load is distributed over a width of 10 cm, for an average heat load of 450 W/cm^2. When a safety factor is added for local hot spots, this heat load is quite severe, and is a major problem of electrostatically

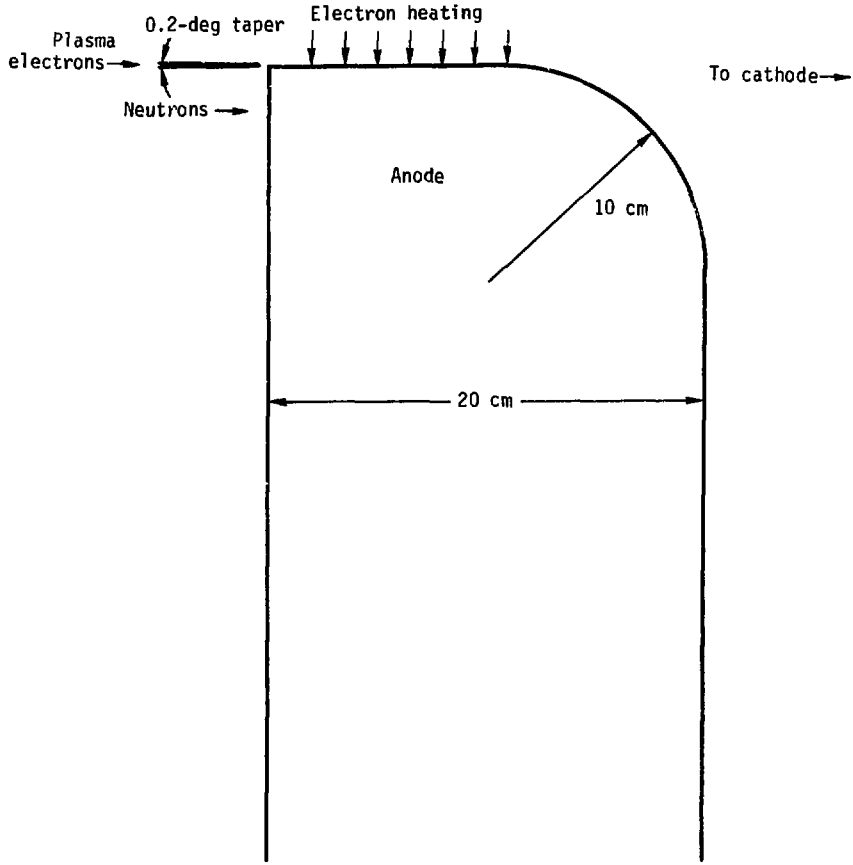

Fig. 29. Detail of anode, showing tapering of leading edge and rounding of trailing edge.

plugged cusp reactors. The front surface of the anodes will receive a heat load of about 0.3 W/cm^2 from neutrons streaming through the collimator and 2 W/cm^2 from bremsstahlung.

If the anode heat load proves to be too high, it can be reduced by about a factor of two by doubling the number of cusps for the same surface area, which would double the anode area. In the terminology of the Magnet Coils

section, this would mean charging from N = 6 to N = 12, and from b = 3 m to b = 0.

Plugging Cathodes

The cathodes are located 60 cm behind the anodes, and are 8 cm apart, which ensures that no primary radiation streaming through the collimators strikes them. The cathodes are supported on 16-cm diam tubes, which pass through feedthroughs immersed in insulating oil. All corners are rounded to radii of at least 10 cm. The maximum electric field on any surface is less than 30 kV/cm.

High voltage electrostatic separators have operated successfully with considerably higher electric fields. Electric fields of 100 kV/cm can be maintained across a 5-cm gap with bare metallic electrodes, and higher voltages can be held if an oxide coating is used on the cathode.[28]

The variation of breakdown voltage vs pressure for stainless steel electrodes with a 20-cm gap is shown in Fig. 30. This figure indicates that accidental excursions in pressure at the electrodes up to 0.013 Pa (10^{-4} Torr) will not impair voltage holding. The voltages that can be maintained in the fusion reactor will be lower than those shown in Fig. 30 for two reasons: radiation and large electrode area. The breakdown voltage

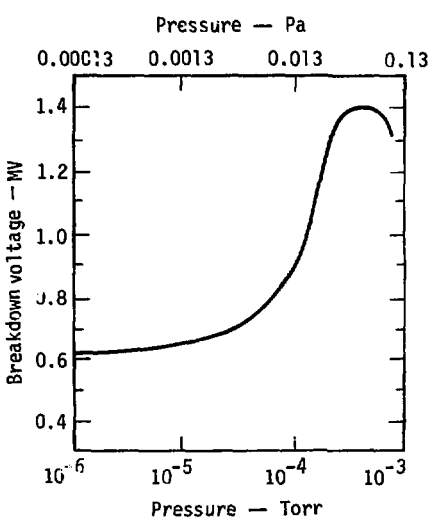

Fig. 30. Variation of breakdown voltage with pressure for polished stainless steel electrodes with a 20-cm gap (from Ref. 28).

decreases gradually with increasing electrode area, probably because of the statistical probability of finding surface flaws.

Radiation causes sputtering and blistering, which can roughen the surface of electrodes and reduce the breakdown voltage. However, Miley has shown that proper conditioning (such as heating and discharge cleaning) can restore the breakdown voltage almost to the original level.[29]

If experiments indicate that the geometry of Fig. 28 will not hold voltage in the presence of plasma radiations, then the more reliable, but more complex, geometry of Fig. 31 can be employed. This latter geometry utilizes the principle of graduating the potential, as is done in accelerator design.

Photons incident on the cathode can eject electrons by secondary emission and photoemission. The bremsstrahlung radiation incident on the

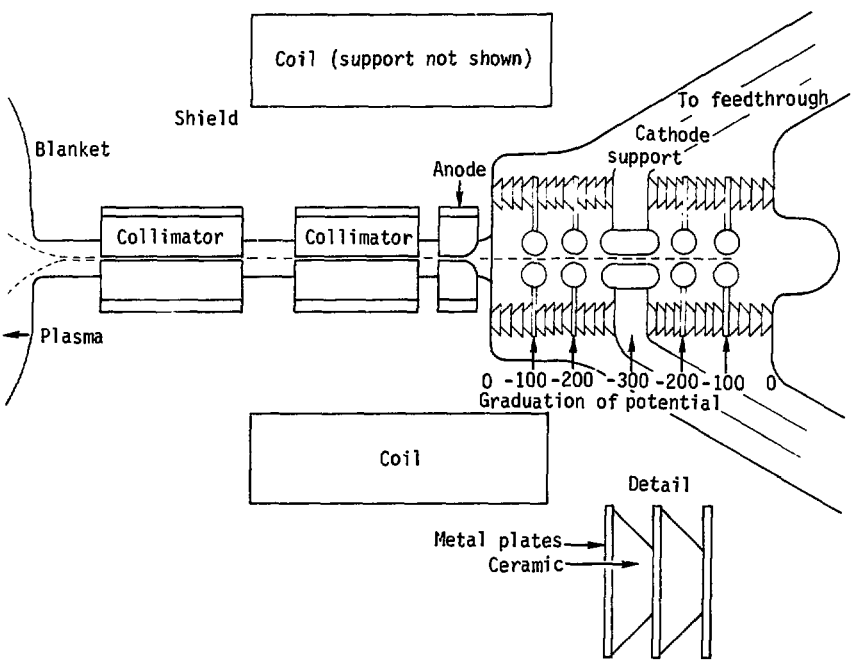

Fig. 31. Alternate design of plugging cathodes employing graduated potential to prevent breakdown.

back wall at W (Fig. 28) has a power density less than 2 W/cm^2 over a height of 1 cm. If all this radiation were backscattered isotropically, the radiation on the back side of the cathodes would be 4.2 mW/cm^2. For an average photon energy of 10 keV, this represents a photon flux of 2.6×10^{12} photons/cm^2 s. If every one of these photons ejected an electron from the cathodes, a current density of 0.42 $\mu A/cm^2$ would result. The total area of the back side of the cathodes is:

$$A_b = 2N2\pi Rh_c \simeq 150\ m^2, \tag{61}$$

where $h_c \simeq 0.2$ m is the effective height of the curved cathode back side. Thus the total photoemission current would be on the order of 0.64 A, which could easily be handled by the power supplies, provided that it did not lead to breakdown.

The plugging cathodes must be maintained slightly more negative than the electron gun cathodes, to ensure that escaping electrons go to the electron gun cathodes and do not escape between the plugging cathodes to the walls.

Electron Guns

The injected electron beam provides the main energy input to sustain plasma temperatures. The beam should be aimed along the magnetic field symmetry plane so that it goes directly into the plasma, and does not get trapped in the magnetic boundary layer. The electron guns are set back several meters from the anodes, where the magnetic field is weaker, in order to make it easy to select the desired field lines for beam injection, as shown in Fig. 32. The guns are located in between the coil support hoops, on the two cusps adjacent to the outermost cusp, which contains the ion collector (to be described next). The total length available for the electron gun cathodes is $L_c = 2(1/2)2\pi R_c \simeq 97$ m, where $R_c = 15.5$ m is the cathode radius, the factor of 2 represents two cusps having electron guns, and the factor of 1/2 allows room for the coil support hoops between electron guns. Because the injected electron current is 1.76 kA, the required emission from the electron guns is 18 A/m, or 180 mA/cm.

The heat deposited per unit length of the cathodes by ion bombardment is:

$$P/L_c = (1 - f_c)n_i V e\phi_A/\tau_{vi}L_c\ , \tag{62}$$

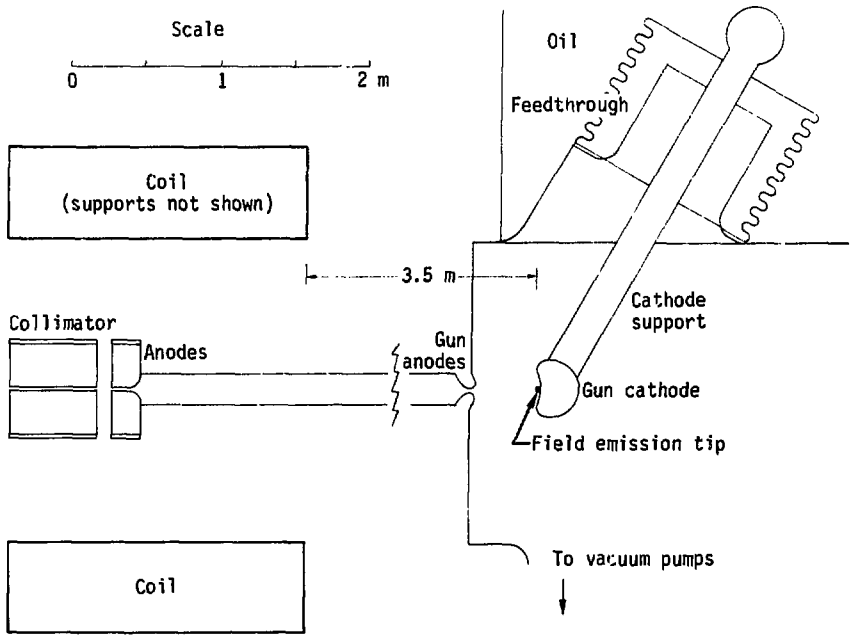

Fig. 32. Field emission electron guns (magnetic field at gun is ∿1 T).

where f_c is the fraction of escaping ions collected by the ion collector. With $f_c = 0.95$, and using parameters to be presented in the next section* and Appendix A, the result is $P/L_c = 7.1$ kW/m, which can be removed by cooling water or oil.

No electron guns like these have ever been built. Pulsed electron guns using field emission attain very high current densities, but "gap closure" (breakdown caused by plasma production) prevents sustaining long pulses. At the other extreme, field emission microscopes operate continuously at lower voltages for hours, but do not provide high currents. Because the electron gun for the present application has not yet been designed, it remains a major uncertainty.

*See Table 3.

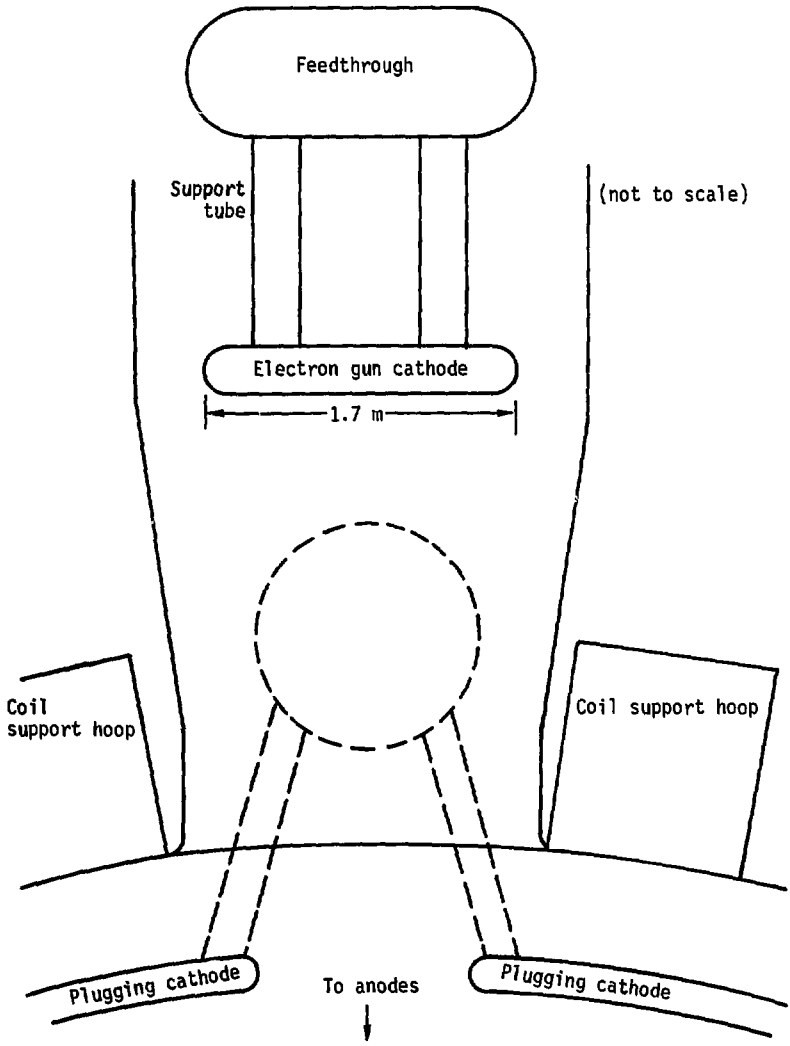

Fig. 33. Top view of electron gun chamber, showing location of gun relative to coil support hoops.

Each electron gun cathode is 1.7 m long and is supported by two tubes mounted on the same feedthrough. Cathodes may be replaced by removing the feedthrough and cathode assembly as a unit. Cathode life has not been estimated. Figure 33 shows how the electron gun cathodes fit in between the coil support hoops. The plugging cathodes located inside the hoops are supported by a feedthrough out of the plane of this drawing (dashed lines), which was not shown in Fig. 32.

Electron gun cathodes will be aligned as follows: with the magnetic field on, the beam from one cathode will be detected with probes located on the inner wall of the plasma chamber. If the beam is following the magnetic field lines to one side or the other as it emerges from the cusp, the cathode can be moved up or down slightly until the beam is centered around the magnetic field symmetry plane. Then most of the injected electrons will be able to enter the nonadiabatic plasma region, as desired. Moving the cathode by 2 mm will shift the electron stream position inside the anodes by about 0.2 mm, which should be a satisfactory tolerance.

After startup of the plasma, the space charge of returning electrons will tend to create a virtual cathode in front of the gun. Then the electron current will be self-regulating, and governed roughly by Child's law. Current can be regulated by adjusting the anode-cathode spacing.

The gun will be situated such that the primary radiation passing through the collimator and hitting the cathode ejects electrons only on field lines that do not intersect the anodes, but go through the anodes to the plasma region or plasma boundary region. It is possible to keep the electrons from hitting the anodes if the magnetic field lines diverge faster than the collimation angle (Fig. 34).

Ion Collectors

The ion collectors, shown in Fig. 35, are located around the outside cusp (Figs. 36 and 37). Here escaping ions are collected at a potential of -90 kV (instead of being collected by the cathodes). Thus, the input electrical power and the heat load on the cathodes are reduced.

Plugging cathodes are located under the coil support hoops, and the ion collectors and their cathodes are set back several meters, as are the electron gun cathodes in Fig. 33. Locating the ion collectors far from the anodes allows the plasma to expand along diverging magnetic field lines. Such a location also allows room for a big vacuum pumping chamber.

Ions emerging from plugging cathodes are repelled by the grounded wall (point W of Fig. 28), and they return through the anode to the plasma. Only ions emerging through the electron gun ports or ion collector ports are removed from the plasma (plus a few that become trapped in the plugging cathode regions and diffuse to the plugging cathodes). The ratio of the flux of ions impinging on the electron gun cathodes to the flux of ions impinging on the ion collector is determined by the anode gaps in front of those electrodes. If the anode gap in front of the electron gun cathodes is made slightly narrower, about 95% of the ions will be lost to the ion collectors before they acquire enough energy to pass through the narrower anode gap in front of the electron gun (not to be confused with the accelerating anodes located close to the electron gun cathode, which have a much wider gap).

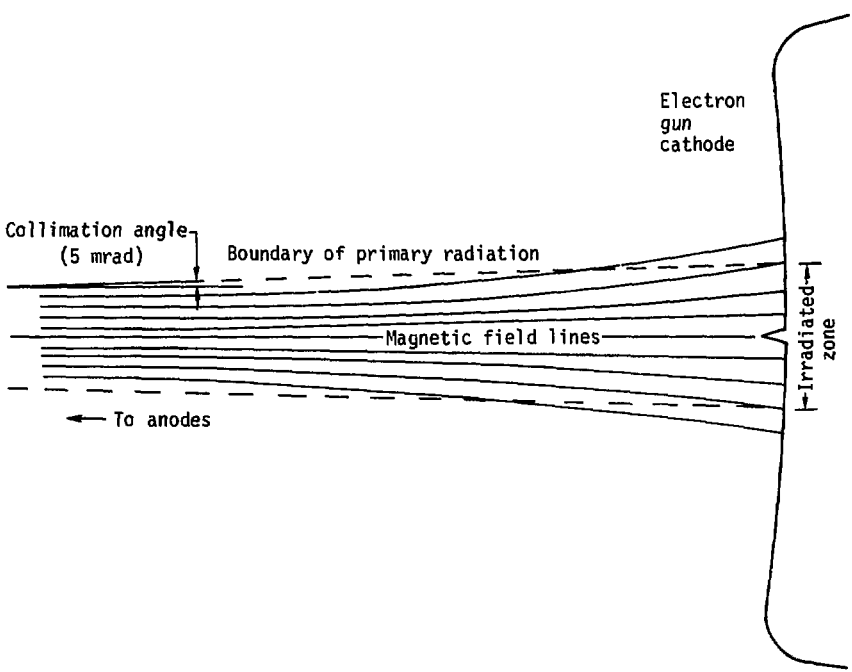

Fig. 34. Divergence of magnetic field lines near electron gun cathode (secondary electrons from irradiated zone will pass between anodes, avoiding breakdown).

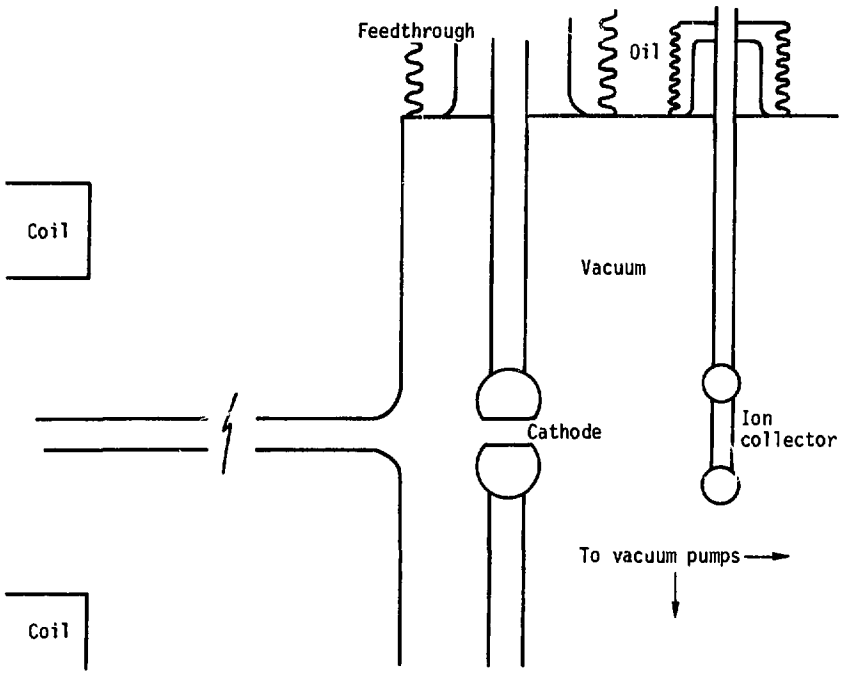

Fig. 35. Ion collector and pumping chamber.

The heat load on the ion collectors is:

$$P_{ic} = n_i^2 g_i e |\phi_{ic} - \Delta\phi| V \ , \tag{63}$$

where ϕ_{ic} is the potential of the ion collector. For the present design, we choose $\phi_{ic} - \Delta\phi = 20$ kV, to ensure collection of ions in spite of variations of $\Delta\phi$ in various anode gaps. For the chosen operating parameters, $\tau_{vi} = (n_i g_i)^{-1} = 458$ s; therefore, $P_{ic} = 0.9$ MW. This heat load is spread over a total collection area of:

$$S_{ic} = (1/2) 2\pi R_{ic} h_{ic} = 7.9 \text{ m}^2 \ , \tag{64}$$

where the factor of 1/2 allows room for coil support hoops, $R_{ic} = 25$ m is the

ion collector radius, and $h_{ic} \simeq 0.1$ m is the height over which the ion stream is spread. Thus, the heat load on the ion collector is $P_{ic}/S_{ic} = 11\ W/cm^2$.

The number of ions neutralized per second is equal to:

$$Q_m = n_i V/\tau_{vi} = 2.9 \times 10^{20}\ \text{atoms/s}\ , \qquad (65)$$

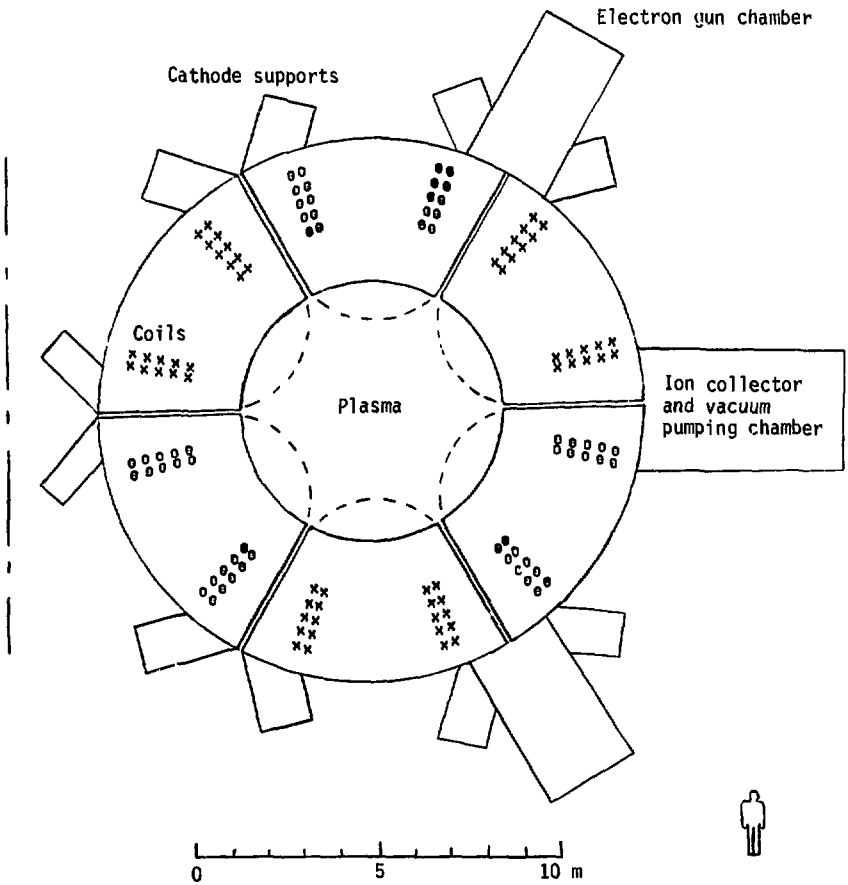

Fig. 36. Cross section of torus, showing arrangement of electrode support chambers.

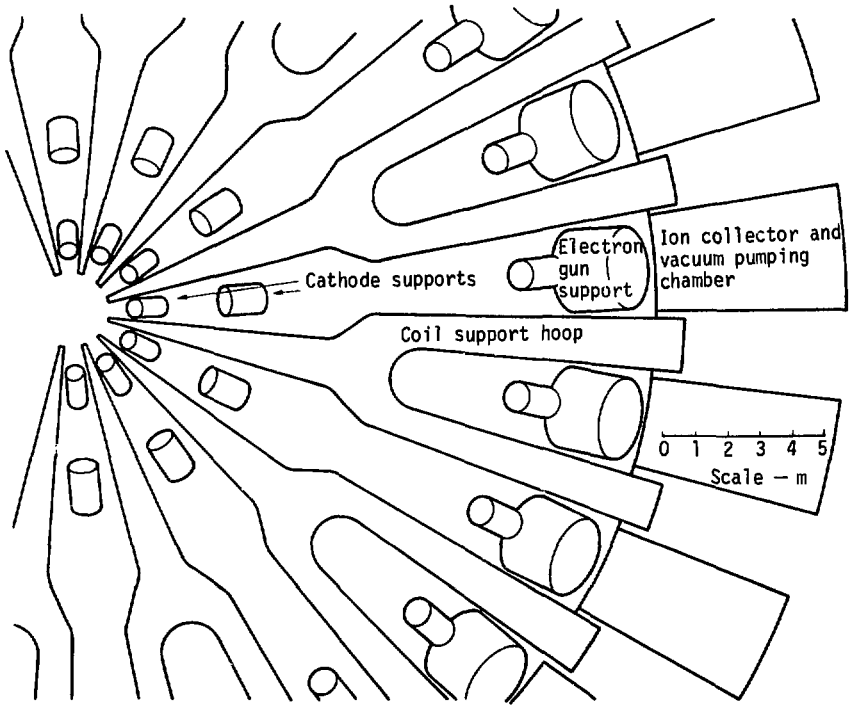

Fig. 37. Top view of torus, showing placement of ion collector and vacuum pumping chambers, electron gun chambers, and cathode supports.

which is the required throughput of the vacuum pumping system. The pumping load is distributed among 24 ion collection chambers, so that the pumping load per chamber is 1.2×10^{19} atoms/s $\approx$ 0.047 Pa-m^3/s. To maintain a pressure in the range of 0.00133 Pa (10^{-5} Torr) requires a pumping speed of:

$$S_p = Q_m/p_m = 35 \text{ m}^3/\text{s} , \tag{66}$$

in each pumping chamber.

Insulators

The alumina feedthroughs are subject to radiation damage. It is not yet known what fluence can be safely withstood, but the limit is probably around

2×10^{21} cm^{-2}.[30] The neutron flux and power at the first wall of the reactor are 7.2×10^{13} $cm^{-2}s^{-1}$ and 1.6 MW/m^2. The attenuation in the collimators can be estimated from the equation[31]:

$$\phi_c/\phi_0 = W/\pi Z \ , \tag{67}$$

where W is the slot width (= 1 cm) and Z is the duct length (= 200 cm). The incident flux is assumed to have a cosine angular distribution. The resulting attenuation factor is 1.6×10^{-3}. In addition, the flux decreases geometrically by a factor of about 100 as it spreads out in the cathode region and backscatters off the wall towards the insulators. Thus, the incident flux is reduced to around 10^9 $cm^{-2}s^{-1}$ at the insulators. If the above fluence limit is correct, the insulator life will be 2×10^{12} s, which is more than adequate.

Reactor Operation

Gas Feed Rate

The plasma acts as a giant vacuum pump, ionizing incident neutral atoms at its surface, heating the ions, and expelling them over the potential barrier to the ion collectors. If neutral gas were not admitted constantly to the chamber, the plasma density would diminish at the rate at which ions are lost. Thus, the plasma density can be controlled by the neutral gas feed rate.

In addition to the primary neutral flux, I_0, from the gas feed system, there are secondary neutrals from charge exchange and reflux off the walls, tertiary neutrals, etc. Each primary neutral produces f_x secondary neutrals, f_x^2 tertiary neutrals, etc., so that the total neutral flow rate is given by[32]:

$$I = I_0 + I_0 f_x + I_0 f_x^2 + I_0 f_x^3 + \ldots = I_0/(1 - f_x). \tag{68}$$

The computer code input, I, was varied to find the neutral influx that gives the optimum Q and net power output, P_{net}.

The variation of n_i, T_i, and Q with I/V is shown in Fig. 38. From the observed optimum value, $I = 6.6 \times 10^{21}$ neutrals/s. Since $f_x = 0.634$, the required gas feed rate is $I_0 = 2.4 \times 10^{21}$ s^{-1}. If the neutral gas feed rate

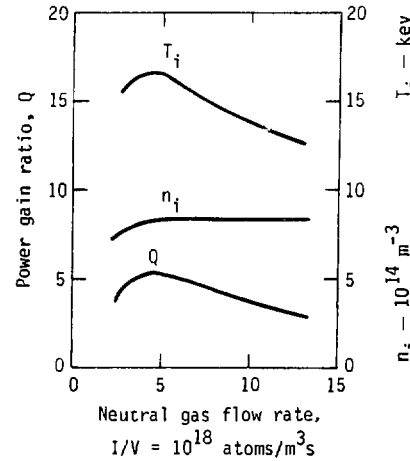

Fig. 38. Variation of T_i, n_i, and Q with neutral gas flow rate, I/V.

is too high, charge exchange lowers the ion temperature and Q; if the gas feed rate is too low, the plasma density drops, again reducing Q.

Power Balance

The power flow diagram for the reactor is shown in Fig. 39, assuming a blanket energy gain of 1.2 and an efficiency of 0.4 for conversion of thermal energy into electricity. The plant efficiency, which is defined as the ratio of net electrical power output to thermal power produced by nuclear reactions, is 0.29.

The main parameters of the reactor are listed in Appendix A.

Startup

Initially the cathodes must be processed with repeated breakdowns until they are conditioned to withstand the design voltage of 300 kV. The conditioning process gradually removes minute surface irregularities that lead to breakdown. Conditioning can be aided by a glow discharge in hydrogen and by rf heating of plasma in the electrode regions.

When the coils have been energized, the anodes and electron gun cathodes are aligned, as described previously. Then an initial filling of deuterium-tritium fuel gas is admitted to the chamber and the electron guns are turned on.

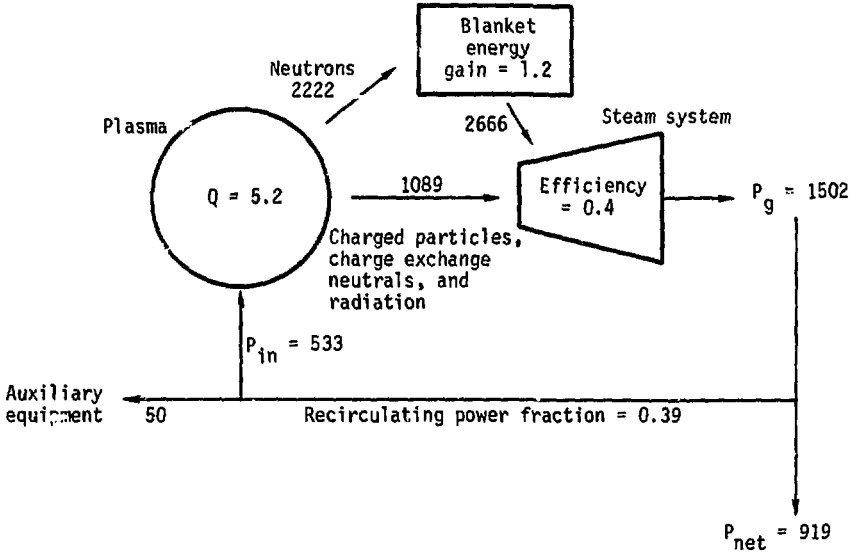

Fig. 39. Power flow diagram for reactor.

As the electron beams enter the chamber, they bounce around and create a plasma by ionization of neutral gas. It is desirable to increase the plasma density rapidly, in order to minimize the equipartition time for ion heating. The rate of density buildup is controlled by the beam injection energy, the initial filling pressure, and the neutral gas feed rate. The time scales for plasma processes at equilibrium are listed in Table 3 (the values of these characteristic times will be considerably different during buildup).

Density buildup from zero density has not been studied, but time integration of the conservation equations, using the second method described in the Theory section under Conservation Equations, indicates that the time scale for approach to equilibrium is on the order of 10 s. Therefore, the startup time will be about 20 s.

Once equilibrium is reached, fusion burn will occur until Q is substantially lowered by impurity buildup, when the reactor will be shut down and flushed out.

Table 3. Time scales for plasma processes.

Density replacement by beam injection	$\tau_b = n/S_b = 13$ s
Density replacement by ionization (at normal gas feed rate)	$\tau_{ion} = n/f_i S_m = 57$ s
Electron-ion equipartition time	$\tau_{eq} = 1.1$ s
Characteristic time for electron-ion collisions causing diffusion	$1/\nu_D = 0.19$ ms
Electron spatial diffusion loss time	$\tau_d = 19$ s
Electron anode trapping time	$\tau_t = 35$ s
Ion velocity-diffusion loss time	$\tau_{vi} = 460$ s
Ion fusion time	$\tau_f = 66$ s
Ion energy loss by charge exchange time	$\tau_x = 33$ s
Ion energy replacement, by ionization and acceleration of new ions, time $\tau_{ia} = 2\alpha_i \phi_i \tau_{ion}/3T_i$	$= 97$ s

Operating Cycle

The rate of impurity buildup is determined by the wall erosion rates from sputtering, blistering, and vaporization. If the surface temperature is kept low enough, vaporization will be negligible. For a preliminary estimate of impurity buildup, we will consider a niobium wall, since sputtering data are readily available for niobium. In order to keep $Z_{eff} < 5$, the impurity fraction must be kept below 0.0027. The numbers of particles incident on the walls (that is, the product of particle fluxes and wall area) are shown in Table 4, along with approximate sputtering yields. The resultant total sputtering yield is about 2.3×10^{18} atoms/s, with the major contribution from the impact of deuterium-tritium atoms from charge exchange.

For a plasma volume of 1.47×10^3 m^3, this sputtering rate represents an impurity density buildup rate of 1.56×10^{15} m^{-3} s^{-1}. The time required for an impurity fraction of 0.0027 to accumulate is therefore about 170 s, ignoring blistering.

In practice, the wall will probably be made out of a lower-Z material, for which the sputtering rates are higher, but the allowable impurity fraction is also larger. The sputtering data on low-Z materials are scant, except for graphite, for which sputtering by 3.5 MeV alpha particles appears to be excessive.[30]

Table 4. Impurity source rates from sputtering of niobium wall (sputtering yields from Ref. 33).

Incident particle species	Number of particles/s	Sputtering yield	Impurity source rate (atoms/s)
3.5 MeV alphas	6.25×10^{20}	0.0005[a]	3.13×10^{17}
25 keV deuterons and tritons	3.93×10^{20}	0.005	19.7×10^{17}
14 MeV neutrons	6.25×10^{20}	10^{-5}[a]	negligible
		Total	2.3×10^{18}

[a]Extrapolated.

After startup, the value of Q will initially be large (greater than 5). Then, as Z_{eff} increases, Q will gradually decrease. When the value of Q gets uneconomically low, the pulse will be terminated by shutting off the neutral gas feed and reducing the cathode voltage. Then the chamber will be flushed with neutral gas and pumped down, and the plasma will be restarted.

The operating cycle thus consists of a startup period lasting about 20 s, followed by a burn period lasting about 200 s, followed by a flush and pumpdown period lasting about 20 s. The first wall material will be chosen to maximize the burn period (and to obtain a satisfactory first-wall lifetime).

Vacuum Pumping

Most of the plasma ions, including impurities, will escape out the cusps when the plasma is turned off. The remaining impurities will be flushed out by flowing neutral gas.

The plasma will be connected to each of these pumping chambers by two rectangular ducts, 0.5 m × 1.5 m × 8.4 m long, as illustrated in Fig. 40. A flap valve is closed to prevent backstreaming during plasma operation and opened to facilitate pumping the plasma chamber during the flushing period. The flow will be in the viscous flow regime during flushing, for which the total conductance of the 48 ducts is calculated to be 3750 P_{avg} m^3/s, where P_{avg} is the average pressure (Pa).

During flushing a throughput of about 3.5×10^{22} molecules/s will be used, which will replace the gas several times in 20 s. This throughput will

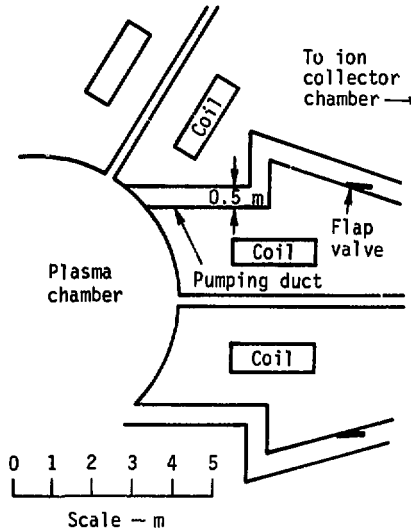

Fig. 40. Pumping ducts for evacuating plasma chamber.

cause a pressure difference of about 0.27 Pa (0.002 Torr) between the plasma chamber and the pumping chambers. If the pressure in the pumping chambers is ~0.013 Pa (0.0001 Torr), the total pumping speed required is about 10^4 m^3/s, which is an order of magnitude larger than the total pumping speed required during operation.

Each of the 24 pumping chambers (ion collection chambers) will have cryopumps backed up by turbomolecular pumps. Diffusion pumps are avoided, because accidental leakage of pump oil or mercury vapor into the electrode regions might cause high voltage breakdown.

Capital Costs

It would be premature to attempt a cost study of electrostatically plugged cusp fusion reactors based on the present brief analysis. However, it is appropriate to compare the coil and structure masses required here with those of other fusion reactor designs for which thorough cost analyses have been made.

These parameters are compared in Table 5. The coil current and structural mass for the cusp lie in between the corresponding values for the mirror hybrid and for the PPL Tokamak reactor design. If we had assumed a

Table 5. Comparison of coils and structure.

	Mirror hybrid fusion-fission reactor (Ref. 22)	Electro-statically plugged cusp reactor	PPL Tokamak reactor (Ref. 24)
Coil current × length, 10^{10} A m	1.08	2.3	2.46
Coil support structural steel, 10^6 kg	19.5	∿8	4.1
Total capital cost (thousands of dollars)	1.21	not estimated	1.22
Net electrical power, MW	611	766	2030

blanket multiplication factor and conversion efficiency of 1.68 and 0.43 (as in the Tokamak design) instead of 1.2 and 0.40, the electrical output power would have been 1230 MW, instead of 766 MW. This is about half the power of the Tokamak and twice the power of the mirror hybrid. (The power output of the Tokamak will be substantially reduced if high energy neutral beams are required for fueling.)

Some of the complex systems of Tokamaks and mirrors, such as neutral beam injectors, divertors, ohmic heating systems, and direct converters, will be absent from the cusp reactor. The total capital cost of the cusp reactor will probably be comparable to the capital costs of the mirror hybrid and Tokamak reactors.

Summary and Conclusions

Plasma Theory

The plasma theory is based on the assumptions of a narrow electron density profile in the anodes, a low trapped electron density, and classical electron diffusion in the boundary layer. All these assumptions appear to be met in present experiments, as discussed in the Introduction under Heating and Energy Loss Mechanisms.

If these conditions are met, the present theory indicates that the resulting plasma will have parameters favorable for a fusion reactor. Under optimum conditions, the ion density is 9×10^{19} m^{-3}, and the required electron beam injection current per unit plasma volume is 1 A/m^3.

The ion temperature scales approximately linearly with applied voltage ($T_i/\phi_A \sim 0.05$), and T_i is practically independent of magnetic field strength.

With B = 8 T and $Z_{eff} = 2.4$, the value of Q increases from 2.5 at an applied voltage of 200 kV to a maximum of 6 at 400 kV.

The most important theoretical problem to be solved in the future is the self-consistent computation of the trapped and untrapped electron density distributions in the anode region, including the effects of magnetic and electric fields, atomic collisions, and diocotron oscillations.

The following pessimistic assumptions have been made: (1) point cusps cannot be effectively plugged (see Magnet Coils section under Cusp Geometries Available), (2) there is no focussing effect of injected beams' increasing the plasma density at small radii (as discussed in Ref. 20), (3) the magnetic field trapping time of plasma electrons is short (see Theory section under Spatial Diffusion), and (4) geometric mirror effects do not reduce the anode electron density below the plasma electron density (see Theory section under Trapped Electrons). Violation of any one of these assumptions will result in substantial improvement of the reactor parameters.

Coils and Structure

For a given applied voltage and magnetic field strength, the ratio of fusion power to coil cost is proportional to the ratio of plasma volume, V, to coil volume, V_c. This ratio is larger for cusps than for other fusion concepts. The structural supports for the coils present no unusual difficulties.

The minimum size device is limited by the need for a 1.5-m blanket-shield region inside the coils and a 3-m clearance outside the coils for structure and electrode feedthroughs.

Electrodes

The use of radiation collimators prevents primary neutron and x-ray radiations from impinging directly on the high voltage electrodes, so that the radiation fluxes onto the cathodes are small. High voltage tests in the

presence of such radiation fluxes are needed to determine voltage holding capabilities.

The anode gap must be maintained at 3 ± 1 mm, to maintain high Q plasma operation. Anode heat removal is a significant problem.

Electron guns are needed that can provide a total of 1.8 kA of electrons at 300 kV continuously for long periods of time.

The ion collectors and chambers perform three useful functions: (1) they improve plant efficiency by collecting escaping ions at -90 kV instead of at -300 kV; (2) they greatly reduce the cathode heat load; and (3) they provide for vacuum pumping at a convenient location.

Operating Cycle

Ionization of cold neutral gas supplied to the surface of the plasma sustains the plasma density, and electron beam injection sustains plasma temperatures. The power balance is satisfactory because Q is large.

Startup takes about 20 s, fusion burn lasts about 200 s, and the cycle is completed by a 20-s flushing and pumpdown. The burn period is limited by impurity buildup.

Acknowledgments

This work was inspired by the success of O. A. Lavrent'ev and coworkers with plasma confinement in "electromagnetic traps" at the Khar'kov Physical-Technical Institute. Neil Maron and Juliette Brosing gave advice on computing, and Dick Bulmer and Brendan McNamara helped with understanding MAFCO. Lloyd Mancebo, Asher Blum, Jim Benford, and David Sloan advised on high voltage problems. Ken Marx and Charlie McDowell contributed information on the rates of electron diffusion in velocity space. The entire work has been guided by Ralph W. Moir.

References

1. O. A. Lavrent'ev, *Ann. N. Y. Acad. Sci.* 251, 152 (1975).
2. T. J. Dolan, *ibid.*, p. 358.
3. T. J. Dolan, B. L. Stansfield, and J. M. Larsen, *Phys. Fluids* 18, 1383 (1975).
4. V. L. Sizonenko and K. N. Stepanov, *Sov. Phys. Tech. Phys.* 20, 468 (1976).
5. T. J. Dolan, J. M. Larsen, and B. L. Stansfield, *Can. J. Phys.* 53, 2341 (1975).
6. V. A. Sidorkin and O. A. Lavrent'ev, *Plasma Physics and the Problems of Controlled Thermonuclear Fusion*, Vol. 2, (Academy of Sciences of the Ukrainian SSR, Izd. Naukova Dumka, Kiev, 1971), pp. 247-251.
7. O. A. Lavrent'ev, in *Plasma Physics*, Vol. 3, (Academy of Sciences of the Ukrainian SSR, Izd. Naukova Dumka, Kiev, 1968), pp. 77-147 — Translation: AEC-tr-7002 (Rev).
8. A. A. Ware and J. E. Faulkner, *Nucl. Fusion* 9, 353 (1969).
9. O. A. Lavrent'ev, A. A. Kalmykov, A. V. Georgievskiy, V. E. Ziser, and V. B. Yuferov, *Izv. Akad. Nauk SSSR*, Energitika i transport 6, 54 (1975).
10. S. Ichimaru, *Basic Principles of Plasma Physics, A Statistical Approach*, (W. A. Benjamin, Inc., Reading, Mass., 1973), p. 260.
11. W. A. Perkins and J. C. Brown, *MAFCO - A Magnetic Field Code for Handling General Current Elements in Three Dimensions*, Lawrence Livermore Laboratory, Rept. UCRL-744, Rev. 2 (1966).
12. R. Limpaecher and K. R. MacKenzie, *Rev. Sci. Instrum.* 44, 726-731 (1973).
13. Yu. I. Pankrat'ev, N. A. Tulin, E. F. Ponomarenko, and V. A. Naboka, *Sov. At. Energy* 35, 911 (1974).
14. T. K. Samec, Y. C. Lee, and B. D. Fried, *Phys. Rev. Lett.* 35, 1763-1766 (1975).
15. R. W. Moir, W. L. Barr, and R. F. Post, *Phys. Fluids* 14, 2531 (1971).
16. L. Spitzer, Jr., *Physics of Fully Ionized Gases*, (Interscience Publishers, New York, 1962), Chapt. 5.
17. D. G. Blondin and T. J. Dolan, *J. Appl. Phys.* 47, 2903 (1976).
18. T. J. Dolan and B. L. Stansfield, *Nucl. Fusion* 13, 960 (1973).
19. F. S. Acton, *Numerical Methods That Work* (Harper & Row, New York, 1970), Chapt. 14.

20. B. N. Kozlov, *At. Energ.* 12, 238 (1962).

21. R. L. Freeman and E. M. Jones, *Atomic Collision Processes in Plasma Physics Experiments*, Culham Laboratory, Abingdon, Berkshire, England, Rept. CLM-R-137, (1974).

22. R. W. Moir, *et al*, *Progress on the Conceptual Design of a Mirror Hybrid Fusion-Fission Reactor*, Lawrence Livermore Laboratory, Rept. UCRL-51797, (1975).

23. G. A. Carlson, Lawrence Livermore Laboratory, private communication (1976).

24. R. G. Mills, Ed., *A Fusion Power Plant*, Plasma Physics Laboratory, Princeton University, Princeton, N. J., Rept. MATT-1050, (1974), Chapt. 13.

25. B. Badger, *et al.*, *UWMAK-II: A Conceptual Tokamak Power Reactor Design*, University of Wisconsin, Madison, Rept. UWFDM-112 (1975).

26. C. J. Schwer, *Scaling of a Truss Support Structure for Yin Yang Coils*, Lawrence Livermore Laboratory, Rept. UCID-16800 (1975).

27. C. J. Schwer and G. A. Carlson, *Scaling of FERF C-clamp Structure with Coil Radius and Magnetic Field Strength*, Lawrence Livermore Laboratory, Rept. UCID-16724 (1975).

28. L. L. Alston, Ed., *High Voltage Technology*, (Oxford Press, New York, 1968), Chapts. 4 and 18.

29. G. H. Miley, *Studies of Radiation Blistering Effects on Voltage Holding*, Lawrence Livermore Laboratory, Rept. UCRL-51749 (1975).

30. G. Hopkins, *et al.*, *Fusion Reactor Studies: Potential of Low Z Materials for the First Wall*, Electric Power Research Institute, Palo Alto, Calif., Rept. EPRI 115-2 (1975), pp. 20 and 30.

31. N. M. Schaeffer, *Reactor Shielding for Nuclear Engineers*, U.S. Atomic Energy Commission, Office of Information Services, Rept. TID-25951, (1973), p. 364.

32. T. H. Batzer, *et al.*, *Conceptual Design of a Mirror Reactor for a Fusion Engineering Research Facility (FERF)*, Lawrence Livermore Laboratory, Rept. UCRL-51617 (1974), p. 39.

33. R. Behrisch, *Nucl. Fusion* 12, 695 (1972).

Appendix A. Table of Reactor Parameters

Coil Configuration	
Toroidal multipole cusp with N = 6 cusps	
Magnetic field in cusp	$B = 8$ T
Clearance with major axis	$a_0 = 3$ m
Clearance between opposite coils	$c = 2$ m
Clearance between like coils	$b = 3$ m
Average current density (assumed)	$J = 2.5$ kA/cm^2
Total coil current × length	$= 2.3 \times 10^{10}$ Am
Total coil mass	$= 6.85 \times 10^6$ kg
Coil support structure: cryogenic steel trusses supported by fiberglass compression columns and room temperature steel hoops	
Structural steel mass	$= 8 \times 10^6$ kg
Vacuum Chamber	
Major radius	$R = 10$ m
Minor radius	$a = 3.6$ m
Blanket and shield thickness (assumed)	$= 1.5$ m
Neutron wall loading	$= 1.6$ MW/m^2
First wall: not designed	
Deuterium-tritium neutral gas feed rate, I_0	$I_0 = 2.4 \times 10^{21}$ atoms/s
Electrodes	
Applied voltage	$\phi_A = 300$ kV
Cathode current	$I_e = 1.78$ kA
Anode heat load	$= 365$ MW
Cathode heat load	$= 1$ MW
Plasma Parameters	
Nominal major radius	$R_p = 9.5$ m
Nominal minor radius	$r_p = 2.8$ m
Nominal plasma volume	$V = 1470$ m^3
Assumed impurity	1% aluminum ($Z_{eff} = 2.4$)
Electron density	$n_e = 1.0 \times 10^{20}$ m^{-3}

Fuel ion density	$n_i = 8.9 \times 10^{19}\ m^{-3}$
Electron temperature	$T_e = 17$ keV
Ion temperature	$T_i = 16.5$ keV
Electron potential barrier	$\phi_e = 88$ kV
Ion potential barrier	$\phi_i = 140$ kV
Potential sag in anodes	$\Delta\phi = 72$ kV
Fusion power density	$P_f/V = 1.89\ MW/m^3$
Average electron Larmor radius in cusp	$\rho_e = 6 \times 10^{-5}$ m
Characteristic width of peak of electron density distribution in anodes (assumed)	$2\rho_e$
Ion Larmor radius in boundary layer	$\rho_i = 2.4$ cm
Boundary layer thickness	$\xi_1 = 10$ mm
Debye length	$\lambda_D = 9.7 \times 10^{-5}$ m
Characteristic times of plasma processes:	see Table 3

Operation

Fusion alpha power	= 556 MW
Fusion neutron power	= 2222 MW
Neutron capture power (assuming a blanket multiplication factor of 1.2)	= 444 MW
Thermal power produced by nuclear reactions	P_{th} = 3222 MW
Power gain ratio	$Q = 5.2$
Thermal conversion efficiency (assumed)	= 0.40
Gross electrical power	= 1502 MW
Recirculating power to cathodes	= 533 MW
Auxiliary equipment power (assumed)	= ∿50 MW
Recirculating power fraction	= 0.39
Net electrical power output	P_{net} = 919 MW
Plant efficiency	$P_{net}/P_{th} = 0.29$
Burn period (limited by impurities)	= ∿200 s
Flush and restart time	= ∿40 s
Duty cycle	= ∿0.83